

1 **Senolytic CAR T cells reverse aging-associated defects in**

2 **intestinal regeneration and fitness**

3 Onur Eskiocak^{1,2*}, Saria Chowdhury^{1*}, Vyom Shah^{1*}, Emmanuella Nnuji-John^{1,3}, Charlie
4 Chung¹, Jacob A.Boyer^{4,5}, Alexander S.Harris¹, Jill Habel¹, Michel Sadelain⁶,
5 Semir Beyaz^{1†#}, Corina Amor^{1†#}.

6 ¹Cold Spring Harbor Laboratory; Cold Spring Harbor, NY, USA.

7 ²Graduate Program in Genetics, Stony Brook University; NY, USA.

8 ³ School of Biological Sciences, Cold Spring Harbor Laboratory; Cold Spring Harbor, NY,
9 USA.

10 ⁴ Lewis Sigler Institute for Integrative Genomics and Department of Chemistry, Princeton
11 University; Princeton, NJ, USA.

12 ⁵Ludwig Institute for Cancer Research, Princeton Branch, Princeton, NJ, USA.

13 ⁶ Center for Cell Engineering, Memorial Sloan Kettering Cancer Center, New York, NY, USA.

14
15 * Contributed equally

16 † To whom correspondence should be addressed to: beyaz@cshl.edu and amor@cshl.edu

17 # Lead contact.

18

19

20

21

22 **SUMMARY**

23 Intestinal stem cells (ISCs) drive the rapid regeneration of the gut epithelium to maintain
24 organismal homeostasis. Aging, however, significantly reduces intestinal regenerative capacity.
25 While cellular senescence is a key feature of the aging process, little is known about the *in vivo*
26 effects of senescent cells on intestinal fitness. Here, we identify the accumulation of senescent
27 cells in the aging gut and, by harnessing senolytic CAR T cells to eliminate them, we uncover
28 their detrimental impact on epithelial integrity and overall intestinal homeostasis in natural aging,
29 injury and colitis. Ablation of intestinal senescent cells with senolytic CAR T cells *in vivo* or *in vitro*
30 is sufficient to promote the regenerative potential of aged ISCs. This intervention improves
31 epithelial integrity and mucosal immune function. Overall, these results highlight the ability of
32 senolytic CAR T cells to rejuvenate the intestinal niche and demonstrate the potential of targeted
33 cell therapies to promote tissue regeneration in aging organisms.

34

35

36

37

38

39

40

41

42

43

44

45

46 INTRODUCTION

47 Tissue regeneration is essential for maintaining organismal homeostasis¹. Within the body, the
48 intestinal epithelium is one the highest self-renewing organs². Intestinal stem cells (ISCs), located
49 at the crypts of the intestinal epithelium, are key in this process through their ability to self-renew
50 and differentiate into various intestinal cell types². However, aging significantly impacts them
51 leading to diminished regenerative capacity and a decline in intestinal epithelial function³⁻⁷. A
52 number of strategies have been tested to enhance the activity of ISCs including dietary
53 modifications and small molecules, but the sustainability, safety and long-term effects of these
54 interventions remain unclear⁷⁻¹². Given the high incidence of gut disorders in the elderly¹³ there is
55 a pressing need to develop more targeted and effective strategies to rejuvenate ISC function in
56 aging. Therefore, understanding the cellular basis of this regenerative decline and developing
57 new therapeutic approaches would have broad implications for aging research and healthspan-
58 promoting interventions.

59
60 A key determinant of organismal aging is cellular senescence^{4,14}. Senescence is a stress
61 response program characterized by stable cell cycle arrest and the production of a
62 proinflammatory senescence-associated secretory phenotype (SASP)¹⁵⁻¹⁷. Senescent cells
63 accumulate with age and contribute to the pathophysiology of a wide range of age-related
64 diseases^{14,18-21}. How senescent cells impact tissue regeneration remains an area of active
65 research. On one hand, senescent cells have been shown to promote wound healing²², *in vivo*
66 reprogramming²³ and lung regeneration in response to injury²⁴. Conversely, senescent cells impair
67 skeletal muscle regeneration²⁵ and hematopoietic stem cell activity²⁶. These different outcomes
68 highlight the need to gain a better understanding of the impact of senescent cells on different
69 stem cell niches. In this regard, little is known about the presence and effect of senescent cells in
70 the aging intestine. In addition, exploring how elimination of senescent cells through selective

71 approaches impacts tissue homeostasis is crucial for generating successful therapeutic
72 regenerative strategies.

73

74 We recently developed the first chimeric antigen receptor (CAR) T cells able to specifically
75 eliminate senescent cells efficiently and safely^{27,28}. CARs redirect the effector function of T cells
76 towards a specific cell-surface antigen and are highly selective at eliminating target-expressing
77 cells^{29,30}. Specifically, senolytic CAR T cells recognize and lyse cells that express the urokinase-
78 plasminogen activator receptor (uPAR)^{27,28}. uPAR has been shown to be highly expressed on the
79 surface of senescent cells in multiple models in mice and humans including in natural aging,
80 where uPAR positive cells contribute to the majority of the senescence burden present in aged
81 tissues^{27,28}.

82

83 Here, we set to study the presence and significance of cellular senescence on intestinal fitness
84 during physiological aging and injury. For this, we harnessed senolytic CAR T cells to ablate
85 senescent cells in the intestine, wherein we uncovered their therapeutic potential to promote
86 regeneration.

87

88 **RESULTS**

89 **Age-dependent accumulation of senescent cells in murine and human small intestines** 90 **correlates with decreased intestinal fitness**

91 As a first step to investigate the presence of senescent cells accumulated during physiological
92 aging in the small intestine we performed senescence-associated beta-galactosidase staining
93 (SA- β -gal) in the proximal jejunum of young (3 months old) and old (20 months old mice) and
94 found a significant increase in the number of SA- β -gal⁺ cells with aging (Figure 1A). To further
95 characterize them, we performed RNA in situ hybridization (ISH) for additional markers of

96 senescence such as *Cdkn2a*, encoding the CDK4/6 inhibitor and tumor suppressor p16^{Ink4a} and
97 *Plaur*, the gene for uPAR, and found an age-dependent increase in their co-expression in the
98 small intestine (Figure 1B). Given that the correlation between *Plaur* expression and uPAR surface
99 protein expression is not linear²⁸³¹ we performed flow cytometry on isolated intestinal crypts from
100 young (3 months old) and old (20 months old) mice. As expected, we observed a significant
101 increase in the percentage of cells expressing surface uPAR in the aged intestines compared to
102 young counterparts (Figure 1C). uPAR+ cells were mostly of epithelial origin and were positive for
103 SA-β-gal staining (Figure D-E). To better characterize the cell types that upregulate uPAR surface
104 expression in this setting we isolated uPAR+ and uPAR- cells from aged (20 months old) intestines
105 through FACS and performed single cell RNA sequencing (scRNAseq) (Figure S1A). We profiled
106 9430 uPAR+ and 7379 uPAR- individual cells. Using unsupervised clustering and marker-based
107 cell labelling³², we assigned 10 different cell types which were visualized using Uniform Manifold
108 Approximation and Projection (UMAP) (Figure S1B-C). Analysis of the different populations for
109 uPAR expression indicated that stem cells, enterocytes and macrophages were the most
110 prominent uPAR-expressing populations in the aged small intestine (Figure 1F and S1D).
111 Importantly, when senescent cells were identified using transcriptomic signatures of senescence³³
112 we found that uPAR positive cells constituted a significant fraction of the senescent-cell burden
113 present in aged intestines (Figure 1G and S1E).

114
115 To explore whether a similar accumulation of senescent cells took place in humans we surveyed
116 scRNAseq data from ileal samples of old (65-70 years old) and young (25-30 years old)
117 individuals³⁴ (Figure S1F-J). Similar to our results in mice, we observed that aging led to the
118 accumulation of cells expressing transcriptomic signatures of senescence³³ in the human small
119 intestine (Figure 1H and S1J). Additionally, while we were limited to the analysis of *PLAUR*
120 transcript expression, we found that its levels significantly increased with age paralleling the
121 increase in senescence signatures in this setting (Figure 1I). Indeed, when we performed RNA

122 ISH for *CDKN2A* and *PLAUR* in human middle aged (56 years old) and old (89 years old)
123 individuals we found an age-related increase in cells co-expressing them (Figure 1J). Taken
124 together, these results indicate that uPAR positive senescent cells accumulate in the small
125 intestines of both mice and humans during physiological aging.

126

127 To start elucidating the potential effect of this accumulation of senescent cells in the intestine we
128 employed a mouse model that allows senescent cell imaging through the expression of a
129 luciferase reporter regulated by the p16^{Ink4a} promoter³⁵. Using these p16^{Luc} mice we observed that
130 their senescent cell burden correlated with a decrease in overall intestinal function (Figure 1K-M).
131 Thus, higher levels of bioluminescence correlated with increased intestinal permeability in these
132 animals, decreased organoid forming ability of their crypts and significant changes in their
133 microbiome composition (Figure 1K-M). Collectively, these data point towards a correlation
134 between senescent cell accumulation and decreased intestinal fitness including ISC activity and
135 barrier function.

136

137 **Senolytic uPAR CAR T cells improve age-induced defects in intestinal epithelial integrity**

138 To functionally interrogate *in vivo* the physiological consequences of this age-dependent
139 accumulation of uPAR-positive senescent cells in the intestine, we harnessed CAR T cells to
140 eliminate them. For this, we employed second generation murine uPAR targeting CAR T cells
141 (m.uPAR-m.28z) that express a single-chain variable fragment (scFv) recognizing mouse uPAR
142 and have mouse CD28 as costimulatory domain^{27,36}. uPAR CAR T cells are safe and highly
143 effective at eliminating senescent cells *in vivo* including in the context of aging where a single
144 infusion has been shown to lead to long-term persistence of the senolytic CAR T cells and their
145 effects^{27,28}.

146

147 Thus, we performed studies in syngeneic mouse strains in which uPAR CAR T cells or control
148 untransduced T cells (herein designated UT) from CD45.1 mice were intravenously infused into
149 CD57BL/6 CD45.2 young (3 months old) and old (18-20 months old) mice (Figure S2A). We
150 employed a dose of 0.5×10^6 CAR-positive cells, which we have observed to be optimal for
151 senolytic efficacy and safety balance^{27,28}. In particular, at this dose there is enough elimination of
152 senescent uPAR positive cells to result in phenotypic improvements in multiple models of fibrosis
153 and aging without developing signs of toxicity either in the form of cytokine release syndrome or
154 histological toxicities^{27,28}. Importantly, in this setting and at this dose, uPAR CAR T cells were
155 detected in the intestinal epithelium of the mice 6 weeks after infusion, where they were present
156 in significantly higher numbers in aged animals correlating with the increased expression of
157 surface uPAR in the small intestine with age (Figure 2A and 1C). uPAR CAR T cells predominantly
158 exhibited a cytotoxic effector T cell phenotype (CD8+ and CD44+) (Figure S2B and S2C) with low
159 levels of exhaustion markers, and were activated at this time point (Figure S2D and S2E)
160 suggesting that they were recognizing uPAR positive cells in this tissue. Administration of uPAR
161 CAR T cells indeed led to a significant decrease in the number of uPAR-positive cells as well as
162 a significant reduction in the number of SA- β -Gal positive cells in the small intestines of aged
163 uPAR CAR T-treated mice versus those that received control UT cells (Figure 2B, 2C, 2D).

164
165 Phenotypically, elimination of senescent cells led to improvements in age-related defects in
166 intestinal epithelial integrity. Thus, treatment with uPAR CAR T cells in aged mice significantly
167 rescued age-induced increased intestinal permeability or “leaky gut”³⁷ as measured by decreased
168 plasma levels of FITC-Dextran 4h after oral administration in aged uPAR CAR T treated mice as
169 compared to aged UT-treated animals (Figure 2E). In addition, administration of uPAR CAR T
170 cells led to an increase in the number of proliferating (EdU positive) epithelial cells in the intestinal
171 crypts (Figure S2F and S2G).

172

173 To further explore the impact of uPAR CAR T cells on intestinal regeneration after injury we
174 challenged the mice with 15Gy abdominal irradiation which elicits cytotoxicity, crypt loss and
175 senescence in the intestinal epithelium⁹. Irradiation of young and old UT and uPAR CAR T treated
176 animals induced selective damage to the intestinal epithelium that was followed by a regenerative
177 phase after injury (Figure S2H, 2F-J). As described³⁸⁻⁴⁰, aged UT treated mice tolerated irradiation
178 worse than their younger counterparts exhibiting increased weight loss over time, greater increase
179 in intestinal permeability, lower numbers of proliferating (EdU positive) cells, and higher numbers
180 of apoptotic caspase 3-positive cells (Figure 2F, 2G,2H,2I,2J). Treatment with uPAR CAR T cells
181 significantly reversed these effects, especially in aged mice where the burden of senescent cells
182 was higher, significantly mitigating the age-related decline in regenerative potential following injury
183 (Figure 2F,2G,2H,2I,2J).

184
185 Furthermore, we explored the effects of senolytic CAR T cells in an intestinal injury model of
186 experimental colitis induced by dextran sulfate sodium (DSS) (Figure S2I). In this setting,
187 treatment with uPAR CAR T cells significantly reduced body weight loss, colonic edema and
188 histological severity of the disease compared to controls (Figure 2K,2L,2M).

189
190 Taken together, these results show that the accumulation of uPAR positive senescent cells in
191 aged and injured intestines contributes to decreased epithelial integrity and reduced regenerative
192 capacity. Thus, elimination of senescent cells with uPAR-targeting CAR T cells significantly
193 rescues these defects.

194

195 **uPAR CAR T cells rejuvenate aged intestinal stem cells**

196 To elucidate the basis for the enhanced regenerative effects associated with uPAR CAR T
197 treatment in aged mice, we performed single cell RNA sequencing in young (3 months-old) and
198 old (20 months-old) mice 6 weeks after treatment with 0.5×10^6 of uPAR CAR-positive or

199 untransduced T cells (Figure 3A-H and S3A-H). We profiled 37,829 single cells and identified 12
200 different cell types, which were visualized using UMAP (Figure S3A-B).

201
202 In accordance with previous histological studies, the proportions of the different cell types varied
203 with aging^{38,41}. Specifically, aged intestinal crypts presented a reduced abundance of intestinal
204 stem cells (ISCs) (Figure 3A-B). Importantly, these aged ISCs manifested a significant decrease
205 in the expression levels of well-established stemness genes such as *Lgr4*, *Myc*, *Sox9*, *Olfm4*,
206 *Malat1* and *Ccnd1* suggesting impaired stem cell activity with age (Figure 3C-D)^{5,38,41}.
207 Interestingly, the intervention with uPAR CAR T cells in aged mice overturned this age-related
208 decline in ISCs abundance and stemness gene expression program (Figure 3E-H). Specifically,
209 besides being present at higher proportions, ISCs from aged uPAR CAR T treated mice were
210 significantly enriched in stem cell signature genes compared to aged UT control mice (Figure 3G-
211 H).

212
213 To assay the regenerative potential of these ISCs we performed clonogenic organoid formation
214 assays from epithelial crypts as well as from sorted Epcam-positive (Epcam⁺) cells from the small
215 intestines of young and old, uPAR CAR T or UT-control treated mice 6 weeks after infusion (Figure
216 3I-K). Congruent with previous reports^{5,7,11}, crypts from old mice generated significantly fewer
217 organoids than those from young mice (Figure 3I-K). However, *in vivo* treatment with uPAR CAR
218 T cells rescued the ability of aged crypts or sorted Epcam⁺ cells to efficiently generate organoids
219 (Figure 3I-K). These results highlight the ability of senolytic CAR T cells to enhance ISC activity
220 and regeneration in aged mice.

221
222 To further understand whether the improved regenerative capacity in response to uPAR CAR T
223 cells is due to their direct effects on the ISCs, we compared the stemness gene signature of aged
224 uPAR⁺ and uPAR⁻ ISCs. Interestingly, ISCs expressing surface uPAR protein had significantly

225 lower expression of key stem genes such as *Lgr4*, *Lgr5*, *Sox9*, *Olfm4* and *Ccnd1* than uPAR
226 negative counterparts (Figure 3L,M). Similarly, analysis of *PLAUR* gene expression in aged
227 human ISCs showed that *PLAUR*⁺ ISC have reduced expression levels of genes involved in stem
228 cell activity compared to *PLAUR*⁻ ones (Figure 3N,O). To assess whether *in vitro* elimination of
229 uPAR⁺ cells in intestinal crypts would be sufficient to rejuvenate them, we co-cultured crypts from
230 young (3 months old) and old (20 months old) mice with either untransduced T cells or uPAR CAR
231 T cells (Figure 3P-S). As expected, uPAR CAR T cells preferentially targeted old crypts that harbor
232 more senescent cells (Figure 3P-Q and S3I). Notably, dissociated single cells from uPAR CAR T
233 treated old organoids gave rise to more organoids in secondary subcultures compared to UT old
234 treated controls (Figure 3R-S). Overall, these results suggests that surface uPAR expression
235 identifies dysfunctional ISCs and their elimination with senolytic CAR T cells is enough to
236 rejuvenate the regeneration potential of aged intestinal crypts.

237

238 In addition to ISCs, aging results in deficits in the functions of mature epithelial cell types such as
239 Paneth, goblet, enteroendocrine cells and enterocytes^{5,42,43}. Compared to UT counterparts, *in vivo*
240 treatment with uPAR CAR T cells in old mice elicited gene expression changes in these mature
241 epithelial cell types that correlate with increased functional fitness (Figure S3J-K).

242

243 Collectively, these data support the notion that removal of uPAR positive cells through senolytic
244 CAR T cells enhances overall intestinal function in aging.

245

246 **Senescent cells drive age-induced intestinal epithelial MHC-II upregulation and mucosal** 247 **immune dysfunction**

248 Age-induced defects in intestinal fitness (such as increased permeability and dysbiosis) have
249 been linked to a cumulative and chronic inflammatory state referred to as “inflammaging”⁴³⁻⁴⁶
250 which in turn further exacerbates intestinal functional decline^{37,47}. Indeed, we observed a

251 significant upregulation of the inflammatory response in the small intestine with aging (Figure 4A-
252 B and S4A). Interestingly, we observed that treatment with uPAR CAR T cells in aged animals
253 significantly abrogated the expression of inflammatory response genes suggesting that senescent
254 cells play a key role in the age-related inflammatory state in the intestine (Figure 4C-D and S4B).
255
256 Senescent cells are highly pro-inflammatory in nature and not only secrete cytokines and
257 chemokines as part of their SASP but also upregulate immune interacting surface molecules such
258 as MHC-I^{16,48,49}. In younger organisms, this leads to their clearance by the immune system
259 restoring tissue homeostasis; however, during aging, altered immune function leads to chronic
260 inflammaging⁵⁰. Nonetheless, the exact mechanisms of the interactions between senescent and
261 immune cells are highly tissue and context specific and remain elusive⁵¹. To get a better
262 understanding of the mechanism whereby senescent cells were promoting intestinal inflammation
263 in aging we studied the expression profile of the most differentially expressed genes related to
264 inflammation in aged intestines upon treatment with uPAR CAR T cells (Figure 4D). Among these,
265 genes encoding MHC-II molecules (such as *H2-Ab1*, *H2-Aa* and *Cd74*, which are upregulated in
266 aging (Figure 4B and S4D)) were among the most significantly downregulated in intestinal
267 epithelial cells (including ISC) upon elimination of senescent cells (Figure 4D and S4E). We and
268 others have recently shown that MHC-II expression on ISCs mediates immune-stem cell crosstalk
269 in the intestinal epithelium influencing inflammation, response to infection and anti-tumor
270 immunity⁵²⁻⁵⁵. Interestingly, we found that MHC-II expression was significantly increased on
271 intestinal uPAR-positive senescent epithelial cells in both mice and humans (Figure 4E-F).
272 Expression of MHC-II on senescent cells has been observed to date in two artificial models of
273 oncogene-induced senescence triggered by the overexpression of mutant *Nras*^{56,57}; however,
274 whether senescent cells express functional MHC-II *in vivo* in physiological models such as aging
275 is unknown. To explore whether naturally occurring senescent cells in the intestine could uptake
276 antigens, we orally administered ovalbumin conjugated to Texas red dye to aged animals and

277 examined the percentage of Texas red-positive cells in the intestines of these mice 1 hour after
278 administration. Interestingly, we found that senescent epithelial cells (identified as CD45⁻, Epcam⁺,
279 uPAR⁺) were more likely to take up antigen than non-senescent epithelial cells (CD45⁻, Epcam⁺,
280 uPAR⁻) (Figure 4G). To further study whether senescent cells could not only uptake antigen but
281 also present it on MHC-II molecules and drive CD4 T cell responses, we sorted CD45 negative,
282 Epcam positive uPAR positive or negative cells and co-cultured them with ovalbumin 323-339
283 peptide and OT-II cells (which are specific for OVA 323-339 presented by MHC-II molecules). We
284 observed that senescent cells were indeed able to stimulate OT-II T cell proliferation (Figure 4H).
285 These results suggest that senescent epithelial cells that accumulate in the small intestine during
286 natural aging express elevated levels of MHC-II and are able to uptake and present antigens to
287 CD4 T cells to stimulate their proliferation. Consistent with this observation, uPAR CAR T cell
288 treatment led to decreased expression of markers of immune senescence on endogenous T cells
289 present in the aged intestinal crypts such as senescent CD4 CD153 and PD1 positive cells (Figure
290 4I) and senescent CD28 negative KLRG1 positive T cells (Figure 4J)^{58,59}. In addition, aged
291 animals treated with uPAR CAR T cells presented decreased levels of nonspecific IgA, a marker
292 of gut mucosal aging^{60,61}(Figure 4K); were able to mount better specific immune responses to
293 mucosal vaccines (Figure 4L) and presented a microbiome composition more similar to that of
294 younger animals (Figure 4M).

295

296 Overall, these results support a crucial role for senescent cells in driving chronic intestinal
297 inflammation and mucosal immune dysfunction in aging and identifies epithelial MHCII expression
298 in the aged intestine as a hallmark of mucosal inflammaging.

299

300 **DISCUSSION**

301 Herein we identify for the first time the accumulation of intestinal senescent cells during
302 physiological aging and validate uPAR as a reliable marker of senescence in this setting.
303 Harnessing uPAR-targeting CAR T cells we show that *in vivo* elimination of senescent cells in
304 aged animals significantly improves epithelial integrity and overall intestinal homeostasis. These
305 results suggest that in the context of the aging intestinal stem cell niche and epithelium, senescent
306 cells significantly impair regenerative capacity. Indeed, we identify uPAR expression as a marker
307 of dysfunctional ISCs whose *in vitro* elimination is sufficient to rejuvenate the regenerative
308 potential of aged intestinal crypts.

309

310 Beyond defects in regeneration, the aged intestinal niche is characterized by chronic inflammation
311 and defects in mucosal immunity. Interestingly, in our work we uncover a key role of senescent
312 cells in driving mucosal immune dysfunction and identify epithelial MHC-II expression as a proxy
313 of inflammaging in the gut. Accordingly, elimination of senescent cells by uPAR CAR T cells leads
314 to downregulation of epithelial MHC-II expression and improved overall mucosal immune function.
315 Previous single cell analysis of intestinal epithelial cells identified ISCs subtypes with reduced
316 levels of MHC-II that correlated with enhanced stem cell activity⁵³. Whether elevated MHC-II levels
317 in aged ISCs contributes to their functional deficits warrants further investigation.

318

319 Overall our results have significant therapeutic implications. They represent the first proof-of-
320 concept that senolytic CAR T cells can effectively promote regeneration in the context of intestinal
321 aging, enteritis and colitis. While further work will be needed to ascertain the effect of senolytic
322 CAR T cells in other stem cell niches; their ability to rejuvenate old ISCs and their
323 microenvironment highlights—the promise of immune cell engineering as a new therapeutic
324 modality in regenerative medicine. These findings fit squarely within the emerging landscape of
325 cellular therapy beyond non-cancer conditions where CAR T cells have been shown to have a
326 high therapeutic profile in infectious and autoimmune diseases as well as in fibrosis and

327 senescence-driven pathologies⁶². Future CAR T approaches could be directed against different
328 surface proteins upregulated in dysfunctional stem cell niches; might employ combinatorial
329 strategies^{63,64} or utilize other immune cell types or delivery routes⁶⁵. In addition, the ability of
330 CAR T cells to incorporate safety switches⁶⁶ balances their high efficacy while minimizing
331 potential side-effects. Altogether, the high efficacy of senolytic CAR T cells to rejuvenate intestinal
332 fitness underscores the potential of immune-based cellular therapy to promote tissue
333 regeneration.

334

335 **LIMITATIONS OF THE STUDY**

336 Our study harnesses senolytic CAR T cells to uncover the detrimental impact of senescent cell
337 accumulation on intestinal regeneration. While *in vitro* co-culture of aged intestinal crypts and
338 senolytic CAR T cells is enough to rejuvenate aged ISCs, it is possible that *in vivo* the elimination
339 of senescent cells in other tissues also contributes to the intestinal phenotypes that we observe.
340 Understanding the consequences on regeneration of systemic senolysis could lead to better
341 regenerative strategies. Further studies are also needed to assess whether epithelial plasticity
342 and niche-mediated regulation of regeneration play a role in the the uPAR CAR T-mediated
343 enhancement of stem cell activity. Finally, while we identify epithelial expression of MHC-II as a
344 robust proxy for inflammaging in the aged intestine, the identity of the antigens that are presented
345 and their direct functional consequences remain to be elucidated.

346

347 **ACKNOWLEDGMENTS**

348 We thank C.J. Sherr, D.A.Tuveson, S.W. Lowe, H.V.Meyer, Y.Ho and I.Fernandez-Maestre for
349 insightful discussions. We thank Cold Spring Harbor laboratory (CSHL) Cancer Center Shared
350 Resources (Animal facility, Flow Cytometry, Imaging, Single Cell Sequencing, Organoid and
351 Histology Core Facilities) supported by NCI Cancer Center Support grant 5P30CA045508.

352 Special thanks to Rachel Rubino, Lisa Bianco, Eileen Earl, Michael Labarbera and Jodi Coblentz
353 for outstanding animal care. We thank Claire Regan and Jonathan Preall for technical support in
354 performing scRNAseq. This work was supported in part by Developmental Funds from the Cancer
355 Center Support Grant P30CA045508 (SB and CA) and was performed with assistance from CSHL
356 Shared Resources funded through the Cancer Center Support Grant P30CA045508. In addition,
357 work in SB laboratory was supported by The Oliver S. and Jennie R. Donaldson Charitable Trust,
358 The G. Harold & Leila Y. Mathers Foundation, the STARR Cancer Consortium I13-0052, The
359 Mark Foundation for Cancer Research 20-028-EDV, Chan Zuckerberg Initiative / Silicon Valley
360 Community Foundation 2021-239862 and the CSHL and Northwell Health Affiliation. Work in CA
361 laboratory was supported by the CSHL and Northwell Health Affiliation, a Longevity impetus grant
362 from Norn Group, National Institutes of Health Common Fund grant 1DP5OD033055-01, National
363 Institute of Aging 1R01AG082800-01.

364

365 **AUTHOR CONTRIBUTIONS**

366 O.E., S.C., V.S., designed, performed and analyzed experiments and edited the manuscript. E.N.,
367 C.C., J.A.B., A.H. J.H. performed experiments and edited the manuscript. MS advised and edited
368 the manuscript. S.B. conceived the project, acquired funding, designed, supervised and analyzed
369 experiments and edited the manuscript. C.A. conceived the project, acquired funding, designed,
370 performed, analyzed and supervised experiments and wrote the paper with assistance from all
371 authors. All authors read and approved the paper.

372

373 **DECLARATION OF INTERESTS**

374 S.B. received research funding from Caper Labs, Elstar Therapeutics and Revitope Oncology for
375 research unrelated to this study. S.B. is an advisor for Caper Labs. S.B and C.A. are listed as
376 inventors on a patent application related to the regenerative effects of senolytic CAR T cells

377 (63/510,997). M.S and C.A. are listed as the inventor of several patent applications (62/800,188;
378 63/174,277; 63/209,941; 63/209,940; 63/209,915; 63/209,924; 17/426,728; 3,128,368;
379 20748891.7; 2020216486) related to senolytic CAR T cells. M.S. is also listed on other unrelated
380 patents concerning CAR T technology. M.S. and C.A. are advisors for Fate Therapeutics.

381 **INCLUSION AND DIVERSITY**

382 We support diverse and inclusive research. One or more of the authors of this paper self-identifies
383 as an underrepresented minority in science.

384

385 **STAR METHODS**

386 **Key resources table**

REAGENT or RESOURCE	SOURCE	IDENTIFIER
Antibodies		

PE-uPAR, AF700-Upar BV785-CD45.1 AF488-CD3 BUV395-CD4 PECy7-CD8 BV421-CD62L APCCy7-CD44 BV650-LAG3 BV510-PD1 BV605-CD25 APC-Epcam FITC-CD45 FITC-MHC-II PE-CD153 BV510-PD1 BV711-CD45.2 PE-Texas red-CD28 BUV737-KLRG1 BUV450-Viability ghost die SYTOX Blue dead cell stain DAPI uPAR Anti-goat (HRP) Caspase 3 Anti-rabbit (HRP) Epcam Anti-rabbit (alexa fluor 488)	R&D systems R&D systems BioLegend BioLegend BD Biosciences BioLegend BioLegend BD Biosciences BioLegend BioLegend BioLegend BioLegend BioLegend Invitrogen Invitrogen BioLegend BioLegend BioLegend BD Biosciences TONBO biosciences Thermo Fisher Scientific Sigma R&D systems Vector Laboratories Cell Signaling Technology Vector Laboratories Cell Signaling Technology Invitrogen	FAB531P; ABLH0521021 FAB531N; AFNL0122081 110743; B319039 100210; B364217 563790; 1165066 100722; B282418 104435; B283191 560568; 1083068 125227; B333220 135241; B342120 102035; B354812 118214; B280290 103102; 2041142 11-5321-82; 2442242 12-1531-82; 2504402 135241; B342120 109847; B348415 102124; B376397 741812; 2327039 13-0868-T500; D0868061022133 S34857; 2491422 32670-5MG-F AF534; DCL0622021 MP-7405; ZJ0718 9664S; 22 MP-7401; ZH0609 93790S; 3 A21206;2376850
Chemicals, peptides and recombinant proteins		
Luciferin Cyclophosphamide Dextran sulfate sodium salt FITC-Dextran EdU Chicken ovalbumin OVA-Texas red OVA323-339 Violet Cell tracker Advanced DMEM RPMI Medium 1640 FBS Penicillin:Streptomycin L-glutamine L-glutamine HEPES MEM non-essential amino acids β-mercaptoethanol Sodium pyruvate mouse anti-CD3/28 Dynabeads	GOLDBIO Sigma MP Biomedicals Sigma Thermo Scientific Sigma Fisher Scientific Anaspec Thermo Fisher Scientific Gibco Gibco Corning GeminiBio Gibco Thermo Scientific Thermo Scientific Thermo Scientific Thermo Scientific Thermo Scientific Gibco	LUCK-1G C0768-10G 0216011090 FD4-250MG A10044 A7641-1G O23021 AS-27024 C34577 12491-015 11-875-085 35-010-CV 400-109 25030-081 25030164 15630080 11140076 21985023 11360070 11452D

Matrigel	Corning	356231
N-2 Supplement	Gibco	17502-048
B-27 Supplement	Gibco	17504-044
Recombinant Murine EGF	Peprtech	315-09
CHIR99021	LC Laboratories	C-6556
Y-27632 dihydrochloride	Sigma-Aldrich	Y0503-5MG
N-Acetyl-L-cysteine	Sigma-Aldrich	A9165-5G
Recombinant Murine Noggin	Peprtech	250-38
Recombinant Murine Rspodin	Peprtech	315-32
TrypLE Express	Thermo Fisher Scientific	12604039
Critical commercial assays		
RNAscope probe: mouse uPAR	ACD	448731
RNAscope probe: mouse cdkn2a	ACD	411011-C2
RNAscope probe: human uPAR	ACD	542701
RNAscope probe: human cdkn2a	ACD	310282-C2
Anti OVA IgA ELISA	Chondrex	3018
Total IgA ELISA	Abcam	ab157717
Granzyme B ELISA	Abcam	ab238265
Click-iT™ Plus EdU Alexa Fluor™ 647	Thermo Scientific	C10640
Imaging Kit		
ImaGene Red C12RG lacZ Gene	Molecular Probes	I2906
Expression Kit		
Mouse Pan T cell isolation kit	Miltenyi Biotec	130-095-130
Experimental models: Organisms/strains		
18 months old C57BL/6J	The Jackson Laboratory	000664
3 months old mice C57BL/6J	The Jackson Laboratory	000664
6 weeks old B6.SJL-Ptprc ^a Pepc ^b /BoyJ	The Jackson Laboratory	002014
p16 ^{Ink4A} -Luciferase	NCI mouse repository	NA
Software and algorithms		
FlowJo 10.8.1	FlowJo LLC	
GraphPad Prism V.9.3.1	GraphPad software	
Image J-Fiji	NIH	
BioRender	BioRender	
Illustrator CC 2022	Adobe	

387

388 **Resource availability**

389 Lead contact

390 Further information and requests for resources and reagents should be directed to the
 391 corresponding authors, Dr.Semir Beyaz (beyaz@cshl.edu) and Dr.Corina Amor
 392 (amor@cshl.edu).

393 Materials availability

394 This study did not generate new unique reagents.

395 Data and code availability

396 scRNA-seq data presented in this study will be deposited in the Gene Expression Omnibus and
397 will be made publicly available upon publication. Original code will be uploaded to a publicly
398 available GitHub repository. Requests for materials should be addressed to the corresponding
399 authors.

400 **Experimental model and subject details**

401 Mice and drug treatments

402 All mouse experiments were approved by CSHL Internal Animal Care and Use Committee
403 (protocol number 21-4). All relevant animal use guidelines and ethical regulations were followed.
404 Mice were maintained under specific pathogen-free conditions. The following mice from The
405 Jackson Laboratory were used: 3-month-old C57BL/6J mice (000664), 18 to 20-month-old
406 C57BL/6J mice (000664) and 6-week-old B6.SJL-Ptrc^a Pepc^b/BoyJ (CD45.1 mice) (002014). Mice
407 of both sexes were used at 3 months of age and 18-20 months of age for the aging experiment
408 and females of 6-10 weeks old for T cell isolation. p16^{Ink4A}-Luciferase (B6.Cg-*Cdkn2a*^{tm3.1Nesh Tyr^{c-}}
409 ^{2J}/Nci) were obtained from the NCI mouse repository (strain O1XBT). p16^{Ink4A}-Luciferase mice
410 between 2-16 months of age were used and monitored by bioluminescence imaging with luciferin
411 (Goldbio) using the IVIS imaging system (PerkinElmer) with Living Image software (PerkinElmer).
412 For abdominal irradiation experiments, mice were irradiated locally once with 15Gy in the
413 abdomen with the help of a lead protector device covering the rest of the body. For DSS
414 administration, dextran sulfate sodium salt M.W.36000-50000 colitis grade (MP biomedical;
415 0216011090) was administered in drinking water at 2% for 9 days. For Edu administration, Edu
416 (Thermo Fisher Scientific; A10044) was injected at 0.5 mg/kg 4 hours before euthanasia as
417 described ⁵². For adoptive T cell transfer mice were treated with one intraperitoneal injection of
418 cyclophosphamide 200mg/kg (Sigma;C0768) 18h before T cell injection as described ²⁷.
419 Ovalbumin-Texas red (Thermo Fisher Scientific;O23021) was administered by oral gavage at

420 1mg/kg 1 hour before euthanasia as described⁶⁷. Immunization with ovalbumin was performed
421 by administering 1mg OVA (Sigma; A7641) by oral gavage three times at 1 week intervals as
422 described in⁶⁸. Mice were kept in group housing. Mice had free access to food and water and
423 were fed (PicoLab Rodent Diet 20, LabDiet). Mice were randomly assigned to the experimental
424 groups.

425 **Methods details**

426 Intestinal crypt isolation and flow cytometry

427 As previously reported^{9,52}, small intestine was removed, washed with cold PBS^{-/-}, opened
428 laterally and cut into 3-5mm fragments. Pieces were washed multiple times with ice cold PBS^{-/-}
429 until clean, washed 2-3 with PBS/EDTA (7.5mM), and incubated with mild agitation for 30 minutes
430 at 4C. Crypts were then mechanically separated from the connective tissue by shaking, and
431 filtered through a 70- μ m mesh into a 50 mL conical tube to remove villus material and tissue
432 fragments. Crypts were removed from this step for crypt culture experiments and embedded in
433 MatrigelTM (Corning 356231 growth factor reduced) with crypt culture media. For Epcam⁺ cell
434 isolation, the crypt suspensions were dissociated to individual cells with TrypLE Express (Thermo
435 Fisher Scientific, 12604039) and stained for flow cytometry. Epithelial cells were isolated as
436 SYTOX⁻, CD45⁻ Epcam⁺ with a BD FACS Aria II SORP cell sorter into supplemented crypt culture
437 medium for culture. uPAR⁺ and uPAR⁻ populations were isolated as DAPI⁻, uPAR^{+/-} with a SONY
438 cell sorter(SH800S). For immune phenotyping, dissociated crypt suspensions were stained for
439 flow cytometry. For this, Fc receptors were blocked using FcR blocking reagent, mouse (Miltenyi
440 Biotec). The following fluorophore-conjugated antibodies were used: PE-uPAR (FAB531P, R&D
441 systems, lot ABLH0521021), AF700-uPAR (FAB531N, R&D systems, lot AFNL0122081), BV785-
442 CD45.1 (110743, BioLegend, lot B319039), AF488-CD3 (100210, BioLegend, lot B364217),
443 BUV395-CD4 (563790, BD Biosciences, lot 1165066), PECy7-CD8 (100722, BioLegend, lot
444 B282418), BV421-CD62L (104435, BioLegend, lot B283191), APCCy7-CD44 (560568, BD
445 Biosciences, lot 1083068), BV650-LAG3 (125227, BioLegend, lot B333220), BV510-PD1

446 (BioLegend, 135241, lot B342120), BV605-CD25 (102035, BioLegend, lot B354812), APC-
447 Epcam (118214, Biolegend,lot B280290), FITC-CD45 (103102, BioLegend, lot 2041142), FITC-
448 MHCII (11-5321-82, Invitrogen, lot 2442242), PE-CD153 (12-1531-82, Invitrogen, lot 2504402),
449 BV510-PD1 (135241, BioLegend, lot B342120), BV711-CD45.2 (109847, BioLegend, lot
450 B348415), PE-Texas red-CD28 (102124, BioLegend, lot B376397), BUV737-LRG1 (741812, BD
451 Biosciences, lot 2327039). Ghost UV 450 Viability Dye (13-0868-T100, Tonbo Biosciences lot
452 D0868083018133) or SYTOX Blue dead cell stain (Thermo Fisher Scientific, S34857; lot2491422)
453 or DAPI (Sigma, 32670-5MG-F) was used as viability dye. Flow cytometry was performed on a
454 LSRFortessa instrument (BD Biosciences), and data were analyzed using FlowJo (TreeStar).

455

456 Single cell RNA-seq

457 Two distinct single cell RNA-seq experiments were conducted: one that assessed the effects of
458 CART-cell treatment on young and old mice and one that analyzed sorted uPAR positive or
459 negative cells from aged intestines. In the CAR T-cell treatment dataset a total of 4 replicates per
460 treatment groups (uPAR & UT) with stratified sampling of age and sex (2 males and 2 females
461 per age and treatment group). For the uPAR positive or negative dataset there were 2 replicates
462 including 2 females and 2 males. Single cell datasets for each experiment were independently
463 assessed for data quality following the guidelines described by^{69,70}. Cells with more than 15%
464 mitochondrial transcripts as well as cells that had fewer than 100 feature counts or expressed
465 fewer than 2000 genes were removed. After QC, Seurat (v4.0.3,⁷¹) was used for normalization,
466 graph-based clustering and differential expression analysis. Each dataset was normalized using
467 *SCTransform* and the 2500 most variable genes were identified with *SelectIntegrationFeatures*.
468 All samples were integrated into a singular dataset via using the *PrepSCTIntegration*,
469 *FindIntegrationAnchors*, and *IntegrateData* functions⁷². MAGIC imputation was conducted on
470 integrated data to impute missing values and account for technical noise⁷³. *RunPCA* was
471 implemented on the integrated datasets to identify the top 15 principal components (PCs) that

472 were used for UMAP analysis and clustering. Louvain clustering at a resolution of 1 was
473 implemented. Clusters were labeled in accordance with expression levels of intestinal epithelial
474 subtype signatures identified by³². Senescent cells were identified by first creating metagene
475 scores for senescence using the signatures described by²⁵. Cells expressing the metagene
476 signature greater than the apex of the distribution of expression were deemed to be senescent.
477 Differential expression analysis was conducted using the *FindMarkers* function with the MAST
478 method to evaluate differences within the transcriptome⁷⁴. Wilcoxon rank-sum tests to determine
479 if gene expression was significant was conducted using the *wilcox.test* function in stats (v4.1.0,
480 (R Core Team, 2021)).

481

482 Organoid culture for crypts and isolated cells

483 Isolated crypts were counted and embedded in Matrigel™ (Corning 356231 growth factor
484 reduced) at 5–10 crypts per μl and cultured in a modified form of medium as described previously
485⁷⁵. Unless otherwise stated, Advanced DMEM (Thermo Fisher Scientific, 12491023) with 10%
486 Penicillin:Streptomycin (GeminiBio, 400-109) was supplemented by EGF 40 ng ml⁻¹ (Peprotech,
487 315-09), Noggin 50 ng ml⁻¹ (Peprotech, 250-38), R-spondin 62.5 ng ml⁻¹ (Peprotech, 315-32), *N*-
488 acetyl-L-cysteine 1 μM (Sigma-Aldrich, A9165), N2 1X (Gibco, 17502-048), B27 1X (Gibco,
489 17504-044), Chiron 10 μM (LC Laboratories, C-6556), Y-27632 dihydrochloride monohydrate
490 20 ng ml⁻¹ (Sigma-Aldrich, Y0503). 25 μL drops of Matrigel™ with crypts were plated onto a flat
491 bottom 48-well plate (Corning 3524) and allowed to solidify for 5-6 minutes in a 37°C incubator.
492 Five hundred microliters of crypt culture medium were then overlaid onto the Matrigel™, changed
493 every other day, and maintained at 37°C in fully humidified chambers containing 5% CO₂.
494 Clonogenicity (colony-forming efficiency) was calculated by plating 50–300 crypts per well and
495 assessing organoid formation 3–7 days or as specified after initiation of cultures. Organoids were
496 propagated as previously described^{9,52}. For secondary subculture experiments, primary
497 organoids were separated for a duration of 6 minutes using TrypLE Express (Thermo Fisher

498 Scientific, 12604039) at a temperature of 37°C. The resulting dissociated single cells were
499 counted and plated equally in Matrigel, and left to solidify. The culture medium was refreshed
500 every other day with fresh crypt media, and the organoids were maintained at 37°C in a fully
501 humidified chamber with 5% CO₂.

502

503 Histological analysis

504 Tissues were fixed overnight in 10% formalin, embedded in paraffin and cut into 5- μ m sections.
505 Sections were subjected to hematoxylin and eosin (H&E) staining. Immunohistochemical staining
506 was performed following standard protocols. The following primary antibodies were used: uPAR
507 (AF534, R&D systems, lot DCL0622021) and Caspase 3 (9664S, Cell Signaling Technology, lot
508 22). The following secondary antibodies were used: HRP Horse anti-goat IgG (MP-7405, Vector
509 Laboratories, lot ZJ0718), HRP Horse anti-rabbit IgG (MP-7401, Vector Laboratories, lot ZH0609)
510 and AF488-donkey Anti rabbit IgG (A21206, Invitrogen, 2376850). For detection of EdU the Click-
511 iTTM Plus EdU Alexa FluorTM 647 Imaging Kit (Thermo Fisher, C10640) was used.

512

513 SA- β -Gal staining

514 SA- β -gal staining was performed as previously described⁷⁶ at pH 5.5 for mouse tissues.
515 Specifically, fresh frozen tissue sections were fixed with 0.5% glutaraldehyde in phosphate-
516 buffered saline (PBS) for 15 min, washed with PBS supplemented with 1 mM MgCl₂ and stained
517 for 5–8 h in PBS containing 1 mM MgCl₂, 1 mg ml⁻¹ X-gal, 5 mM potassium ferricyanide and 5
518 mM potassium ferrocyanide. Tissue sections were counterstained with eosin. Three fields per
519 section were counted with ImageJ and averaged to quantify the percentage of SA- β -gal+ area
520 per field. For the fluorescent SA- β -gal labelling, tissue slides were exposed to the C12RG
521 substrate at 37°C according to manufacturer's instructions (ImaGene Red C12RG lacZ Gene
522 Expression Kit, Molecular Probes, I2906)^{77,78}. Subsequently, for IF analysis, slides were fixed with
523 4% PFA for 10 minutes at room temperature and proceed with regular IF as performed following

524 standard protocols and previously described²⁷. The following antibodies were used: anti-mouse
525 uPAR (R&D, AF534, 1:100)

526

527 In situ hybridization

528 Single-molecule *in situ* hybridization was performed to detect Plaur (mouse: 448731; human:
529 542701) and Cdkn2a (mouse: 411011-C2; human 310282-C2) using Advanced Cell Diagnostics
530 RNAscope 2.5 HD Detection Kit following manufacturer's instructions.

531

532 Human samples

533 De-identified human samples from colonoscopy biopsies of patients (males and females between
534 56 and 89 years of age) with a diagnosis of colon adenocarcinoma were obtained through the
535 Northwell Health Biospecimen Repository. All human studies complied with all relevant guidelines
536 and ethical regulations and were approved by the Institutional Review Board at Northwell Health
537 (Protocol number IRB20-0150).

538

539 Intestinal permeability assay

540 Mice were fasted for 6 hours before starting the test and a pre-test plasma sample was collected
541 after this time. Subsequently, mice were administered by oral gavage 150ul of 80mg/ml FITC-
542 Dextran (4kDa) (Sigma-Aldrich; FD4-250mg). Plasma sample collection was repeated 4 hours
543 post-gavage. The pre and post plasma samples were diluted 1:10 in PBS and a total volume of
544 100ul transferred to a black 96 well plate. Pre and post plasma fluorescence levels were
545 determined in a plate reader at 530nm with excitation at 485nm.

546

547 Isolation, expansion and transduction of mouse T cells

548 B6.SJL-Ptcr^a Pepc^b/BoyJ(CD45.1 mice) were euthanized and spleens were collected. After tissue
549 dissection and red blood cell lysis, primary mouse T cells were purified using the mouse Pan T

550 cell Isolation Kit (Miltenyi Biotec; 130-095-130). Purified T cells were cultured in RPMI-1640
551 (Invitrogen; 11-875-085) supplemented with 10% FBS (Corning; 35-010-CV), 10 mM HEPES
552 (Thermo Scientific; 15630080), 2 mM L-glutamine (Thermo Scientific; 25030164), MEM non-
553 essential amino acids 1x (Thermo Scientific; 11140076), 55 μ M β -mercaptoethanol (Thermo
554 Scientific; 21985023), 1 mM sodium pyruvate (Thermo Scientific; 11360070), 100 IU ml⁻¹
555 recombinant human IL-2 (Proleukin; Novartis) and mouse anti-CD3/28 Dynabeads (Gibco;
556 11452D) at a bead:cell ratio of 1:2. T cells were spinoculated with retroviral supernatant collected
557 from Phoenix-ECO cells 24 h after initial T cell activation as described^{79,80} and used for functional
558 analysis 3–4 days later.

559

560 Genetic modification of T cells

561 The mouse SFG γ -retroviral m.uPAR-m28z plasmid has been described²⁷ and was obtained from
562 Memorial Sloan Kettering Cancer Center. In this construct the anti-mouse uPAR scFv is preceded
563 by a mouse CD8A leader peptide and followed by the Myc-tag sequence (EQKLISEEDL), mouse
564 CD28 transmembrane and intracellular domain and mouse CD3z intracellular domain^{79,80}. A
565 plasmid encoding the SFG γ retroviral vector were used to transfect gpg29 fibroblasts (H29) to
566 generate VSV-G pseudotyped retroviral supernatants, which were used to construct stable
567 retrovirus-producing cell lines as described^{79,81}.

568

569 Antigen presentation experiments

570 Were performed as described in⁵³. In brief, 5x10³ sort purified CD45⁻Epcam⁺uPAR⁺ or uPAR⁻
571 cells were cultured with 5x10⁴ OT-II T cells in the organoid culture medium described above
572 (without Matrigel), with or without 15ug/ml ovalbumin peptide (Anaspec; AS-27024) at 37C for
573 72h. T cell proliferation was assessed using the CellTrace Violet proliferation kit (Thermo Fisher
574 Scientific, C34557) per manufacturer's instructions.

575

576 Detection of Granzyme B or IgA levels

577 Levels of granzyme B, total IgA or anti-OVA IgA from mouse plasma were evaluated by enzyme-
578 linked immunosorbent assay (ELISA) according to the manufacturer's protocols (Abcam;
579 ab238265) granzyme B, (Abcam; ab157717) total and (Chondrex, 3018) anti-OVA.

580

581 Taxonomic microbiota analysis/Metagenomics

582 Metagenomics sequencing analysis of fecal samples was performed by Transnetyx (Cordova,
583 TN) as described⁸². Briefly, fresh mouse fecal samples were placed in barcoded sample collection
584 tubes containing DNA stabilization buffer and shipped to Transnetyx where DNA extraction, library
585 preparation, sequencing, and the initial analysis were performed. Raw data files were uploaded
586 to One Codex analysis software.

587

588 **Quantification and statistical analysis**

589 Unless specified statistical analysis was performed using GraphPad Prism v.6.0 or 7.0 (GraphPad
590 software). Flow cytometry data was analyzed with FlowJo 10.8.1 (FlowJo LLC). Images were
591 analyzed with Image J-Fiji (NIH). No statistical methods were used to predetermine sample size
592 in the mouse studies, and mice were allocated at random to treatment groups. Figures were
593 prepared using BioRender.com for scientific illustrations and Illustrator CC 2022 (Adobe).

594

595 **REFERENCES**

- 596 1 Biteau, B., Hochmuth, C. E. & Jasper, H. Maintaining tissue homeostasis: dynamic control
597 of somatic stem cell activity. *Cell Stem Cell* **9**, 402-411, doi:10.1016/j.stem.2011.10.004
598 (2011).
- 599 2 Barker, N. Adult intestinal stem cells: critical drivers of epithelial homeostasis and
600 regeneration. *Nat Rev Mol Cell Biol* **15**, 19-33, doi:10.1038/nrm3721 (2014).
- 601 3 Brunet, A., Goodell, M. A. & Rando, T. A. Ageing and rejuvenation of tissue stem cells and
602 their niches. *Nat Rev Mol Cell Biol* **24**, 45-62, doi:10.1038/s41580-022-00510-w (2023).
- 603 4 Lopez-Otin, C., Blasco, M. A., Partridge, L., Serrano, M. & Kroemer, G. The hallmarks of
604 aging. *Cell* **153**, 1194-1217, doi:10.1016/j.cell.2013.05.039 (2013).
- 605 5 Pentinmikko, N. *et al.* Notum produced by Paneth cells attenuates regeneration of aged
606 intestinal epithelium. *Nature* **571**, 398-402, doi:10.1038/s41586-019-1383-0 (2019).

- 607 6 Kumar, S., Suman, S., Fornace, A. J. & Datta, K. Intestinal stem cells acquire premature
608 senescence and senescence associated secretory phenotype concurrent with persistent
609 DNA damage after heavy ion radiation in mice. *Aging (Albany NY)* **11**, 4145-4158,
610 doi:10.18632/aging.102043 (2019).
- 611 7 Mihaylova, M. M. *et al.* Fasting Activates Fatty Acid Oxidation to Enhance Intestinal Stem
612 Cell Function during Homeostasis and Aging. *Cell Stem Cell* **22**, 769-778 e764,
613 doi:10.1016/j.stem.2018.04.001 (2018).
- 614 8 Yilmaz, O. H. *et al.* mTORC1 in the Paneth cell niche couples intestinal stem-cell function
615 to calorie intake. *Nature* **486**, 490-495, doi:10.1038/nature11163 (2012).
- 616 9 Beyaz, S. *et al.* High-fat diet enhances stemness and tumorigenicity of intestinal
617 progenitors. *Nature* **531**, 53-58, doi:10.1038/nature17173 (2016).
- 618 10 Cheng, C. W. *et al.* Ketone Body Signaling Mediates Intestinal Stem Cell Homeostasis
619 and Adaptation to Diet. *Cell* **178**, 1115-1131 e1115, doi:10.1016/j.cell.2019.07.048 (2019).
- 620 11 Igarashi, M. & Guarente, L. mTORC1 and SIRT1 Cooperate to Foster Expansion of Gut
621 Adult Stem Cells during Calorie Restriction. *Cell* **166**, 436-450,
622 doi:10.1016/j.cell.2016.05.044 (2016).
- 623 12 Beyaz, S., Mana, M. D. & Yilmaz, O. H. High-fat diet activates a PPAR-delta program to
624 enhance intestinal stem cell function. *Cell Stem Cell* **28**, 598-599,
625 doi:10.1016/j.stem.2021.03.001 (2021).
- 626 13 Dumic, I. *et al.* Gastrointestinal Tract Disorders in Older Age. *Can J Gastroenterol Hepatol*
627 **2019**, 6757524, doi:10.1155/2019/6757524 (2019).
- 628 14 Baker, D. J. *et al.* Clearance of p16Ink4a-positive senescent cells delays ageing-
629 associated disorders. *Nature* **479**, 232-236, doi:10.1038/nature10600 (2011).
- 630 15 Sharpless, N. E. & Sherr, C. J. Forging a signature of in vivo senescence. *Nat Rev Cancer*
631 **15**, 397-408, doi:10.1038/nrc3960 (2015).
- 632 16 Lasry, A. & Ben-Neriah, Y. Senescence-associated inflammatory responses: aging and
633 cancer perspectives. *Trends Immunol* **36**, 217-228, doi:10.1016/j.it.2015.02.009 (2015).
- 634 17 Coppe, J. P. *et al.* Senescence-associated secretory phenotypes reveal cell-
635 nonautonomous functions of oncogenic RAS and the p53 tumor suppressor. *PLoS Biol* **6**,
636 2853-2868, doi:10.1371/journal.pbio.0060301 (2008).
- 637 18 Aguayo-Mazzucato, C. *et al.* Acceleration of beta Cell Aging Determines Diabetes and
638 Senolysis Improves Disease Outcomes. *Cell Metab* **30**, 129-142 e124,
639 doi:10.1016/j.cmet.2019.05.006 (2019).
- 640 19 Baker, D. J. *et al.* Naturally occurring p16(Ink4a)-positive cells shorten healthy lifespan.
641 *Nature* **530**, 184-189, doi:10.1038/nature16932 (2016).
- 642 20 Bussian, T. J. *et al.* Clearance of senescent glial cells prevents tau-dependent pathology
643 and cognitive decline. *Nature* **562**, 578-582, doi:10.1038/s41586-018-0543-y (2018).
- 644 21 Childs, B. G. *et al.* Senescent intimal foam cells are deleterious at all stages of
645 atherosclerosis. *Science* **354**, 472-477, doi:10.1126/science.aaf6659 (2016).
- 646 22 Demaria, M. *et al.* An essential role for senescent cells in optimal wound healing through
647 secretion of PDGF-AA. *Dev Cell* **31**, 722-733, doi:10.1016/j.devcel.2014.11.012 (2014).
- 648 23 Mosteiro, L. *et al.* Tissue damage and senescence provide critical signals for cellular
649 reprogramming in vivo. *Science* **354**, doi:10.1126/science.aaf4445 (2016).
- 650 24 Reyes, N. S. *et al.* Sentinel p16(INK4a+) cells in the basement membrane form a
651 reparative niche in the lung. *Science* **378**, 192-201, doi:10.1126/science.abf3326 (2022).
- 652 25 Moiseeva, V. *et al.* Senescence atlas reveals an aged-like inflamed niche that blunts
653 muscle regeneration. *Nature* **613**, 169-178, doi:10.1038/s41586-022-05535-x (2023).
- 654 26 Chang, J. *et al.* Clearance of senescent cells by ABT263 rejuvenates aged hematopoietic
655 stem cells in mice. *Nat Med* **22**, 78-83, doi:10.1038/nm.4010 (2016).
- 656 27 Amor, C. *et al.* Senolytic CAR T cells reverse senescence-associated pathologies. *Nature*
657 **583**, 127-132, doi:10.1038/s41586-020-2403-9 (2020).

- 658 28 Amor, C., Maestre-Fernandez, I., Chowdhury, S., Ho, Y., Nadella, S., Graham, C.,
659 Carrasco, S.E., Nnuji-John, E., Feucht, J., Hinterleitner, C., Barthet, V.J.A., Boyer, J.,
660 Mezzadra, R., Wereski, M.G., Tuveson, D.A., Levine, L.R., Jones, L.W., Sadelain, M.,
661 Lowe S.W. Prophylactic and long-lasting efficacy of senolytic CAR T cells against age-
662 related metabolic dysfunction. *doi.org/10.21203/rs.3.rs-3385749/v1*.
- 663 29 Sadelain, M., Riviere, I. & Riddell, S. Therapeutic T cell engineering. *Nature* **545**, 423-431,
664 doi:10.1038/nature22395 (2017).
- 665 30 Lim, W. A. & June, C. H. The Principles of Engineering Immune Cells to Treat Cancer. *Cell*
666 **168**, 724-740, doi:10.1016/j.cell.2017.01.016 (2017).
- 667 31 Liu, Y., Beyer, A. & Aebersold, R. On the Dependency of Cellular Protein Levels on mRNA
668 Abundance. *Cell* **165**, 535-550, doi:10.1016/j.cell.2016.03.014 (2016).
- 669 32 Haber, A. L. *et al.* A single-cell survey of the small intestinal epithelium. *Nature* **551**, 333-
670 339, doi:10.1038/nature24489 (2017).
- 671 33 Saul, D. *et al.* A new gene set identifies senescent cells and predicts senescence-
672 associated pathways across tissues. *Nat Commun* **13**, 4827, doi:10.1038/s41467-022-
673 32552-1 (2022).
- 674 34 Elmentaite, R. *et al.* Cells of the human intestinal tract mapped across space and time.
675 *Nature* **597**, 250-255, doi:10.1038/s41586-021-03852-1 (2021).
- 676 35 Burd, C. E. *et al.* Monitoring tumorigenesis and senescence in vivo with a p16(INK4a)-
677 luciferase model. *Cell* **152**, 340-351, doi:10.1016/j.cell.2012.12.010 (2013).
- 678 36 Amor, C., Feucht, J., Leibold, J., Sadelain, M., Lowe, S. Senolytic car-t cells targeting upar,
679 a cell surface and secreted senescence biomarker. *WO2020160518A1* (2020).
- 680 37 Man, A. L. *et al.* Age-associated modifications of intestinal permeability and innate
681 immunity in human small intestine. *Clin Sci (Lond)* **129**, 515-527,
682 doi:10.1042/CS20150046 (2015).
- 683 38 Nalapareddy, K. *et al.* Canonical Wnt Signaling Ameliorates Aging of Intestinal Stem Cells.
684 *Cell Rep* **18**, 2608-2621, doi:10.1016/j.celrep.2017.02.056 (2017).
- 685 39 Martin, K., Potten, C. S., Roberts, S. A. & Kirkwood, T. B. Altered stem cell regeneration
686 in irradiated intestinal crypts of senescent mice. *J Cell Sci* **111 (Pt 16)**, 2297-2303,
687 doi:10.1242/jcs.111.16.2297 (1998).
- 688 40 Potten, C. S., Martin, K. & Kirkwood, T. B. Ageing of murine small intestinal stem cells.
689 *Novartis Found Symp* **235**, 66-79; discussion 79-84, 101-104,
690 doi:10.1002/0470868694.ch7 (2001).
- 691 41 Martin, K., Kirkwood, T. B. & Potten, C. S. Age changes in stem cells of murine small
692 intestinal crypts. *Exp Cell Res* **241**, 316-323, doi:10.1006/excr.1998.4001 (1998).
- 693 42 Sovran, B. *et al.* Age-associated Impairment of the Mucus Barrier Function is Associated
694 with Profound Changes in Microbiota and Immunity. *Sci Rep* **9**, 1437, doi:10.1038/s41598-
695 018-35228-3 (2019).
- 696 43 Hohman, L. S. & Osborne, L. C. A gut-centric view of aging: Do intestinal epithelial cells
697 contribute to age-associated microbiota changes, inflammaging, and
698 immunosenescence? *Aging Cell* **21**, e13700, doi:10.1111/accel.13700 (2022).
- 699 44 Franceschi, C., Garagnani, P., Parini, P., Giuliani, C. & Santoro, A. Inflammaging: a new
700 immune-metabolic viewpoint for age-related diseases. *Nat Rev Endocrinol* **14**, 576-590,
701 doi:10.1038/s41574-018-0059-4 (2018).
- 702 45 Jeong, J. H. *et al.* Microvasculature remodeling in the mouse lower gut during
703 inflammaging. *Sci Rep* **7**, 39848, doi:10.1038/srep39848 (2017).
- 704 46 Dugan, B., Conway, J. & Duggal, N. A. Inflammaging as a target for healthy ageing. *Age*
705 *Ageing* **52**, doi:10.1093/ageing/afac328 (2023).
- 706 47 Thevaranjan, N. *et al.* Age-Associated Microbial Dysbiosis Promotes Intestinal
707 Permeability, Systemic Inflammation, and Macrophage Dysfunction. *Cell Host Microbe* **23**,
708 570, doi:10.1016/j.chom.2018.03.006 (2018).

- 709 48 Chen, H. A. *et al.* Senescence Rewires Microenvironment Sensing to Facilitate Antitumor
710 Immunity. *Cancer Discov* **13**, 432-453, doi:10.1158/2159-8290.CD-22-0528 (2023).
- 711 49 Marin, I. *et al.* Cellular Senescence Is Immunogenic and Promotes Antitumor Immunity.
712 *Cancer Discov* **13**, 410-431, doi:10.1158/2159-8290.CD-22-0523 (2023).
- 713 50 Ovadya, Y. *et al.* Impaired immune surveillance accelerates accumulation of senescent
714 cells and aging. *Nat Commun* **9**, 5435, doi:10.1038/s41467-018-07825-3 (2018).
- 715 51 Kale, A., Sharma, A., Stolzing, A., Desprez, P. Y. & Campisi, J. Role of immune cells in the
716 removal of deleterious senescent cells. *Immun Ageing* **17**, 16, doi:10.1186/s12979-020-
717 00187-9 (2020).
- 718 52 Beyaz, S. *et al.* Dietary suppression of MHC class II expression in intestinal epithelial cells
719 enhances intestinal tumorigenesis. *Cell Stem Cell* **28**, 1922-1935 e1925,
720 doi:10.1016/j.stem.2021.08.007 (2021).
- 721 53 Biton, M. *et al.* T Helper Cell Cytokines Modulate Intestinal Stem Cell Renewal and
722 Differentiation. *Cell* **175**, 1307-1320 e1322, doi:10.1016/j.cell.2018.10.008 (2018).
- 723 54 Tuganbaev, T. *et al.* Diet Diurnally Regulates Small Intestinal Microbiome-Epithelial-
724 Immune Homeostasis and Enteritis. *Cell* **182**, 1441-1459 e1421,
725 doi:10.1016/j.cell.2020.08.027 (2020).
- 726 55 Lim, A. I. *et al.* Prenatal maternal infection promotes tissue-specific immunity and
727 inflammation in offspring. *Science* **373**, doi:10.1126/science.abf3002 (2021).
- 728 56 van Tuyn, J. *et al.* Oncogene-Expressing Senescent Melanocytes Up-Regulate MHC
729 Class II, a Candidate Melanoma Suppressor Function. *J Invest Dermatol* **137**, 2197-2207,
730 doi:10.1016/j.jid.2017.05.030 (2017).
- 731 57 Kang, T. W. *et al.* Senescence surveillance of pre-malignant hepatocytes limits liver cancer
732 development. *Nature* **479**, 547-551, doi:10.1038/nature10599 (2011).
- 733 58 Yoshida, S. *et al.* The CD153 vaccine is a senotherapeutic option for preventing the
734 accumulation of senescent T cells in mice. *Nat Commun* **11**, 2482, doi:10.1038/s41467-
735 020-16347-w (2020).
- 736 59 Zhang, J., He, T., Xue, L. & Guo, H. Senescent T cells: a potential biomarker and target
737 for cancer therapy. *EBioMedicine* **68**, 103409, doi:10.1016/j.ebiom.2021.103409 (2021).
- 738 60 Mabbott, N. A. *et al.* Aging and the mucosal immune system in the intestine.
739 *Biogerontology* **16**, 133-145, doi:10.1007/s10522-014-9498-z (2015).
- 740 61 Kawamoto, S. *et al.* Bacterial induction of B cell senescence promotes age-related
741 changes in the gut microbiota. *Nat Cell Biol*, doi:10.1038/s41556-023-01145-5 (2023).
- 742 62 Baker, D. J., Arany, Z., Baur, J. A., Epstein, J. A. & June, C. H. CAR T therapy beyond
743 cancer: the evolution of a living drug. *Nature* **619**, 707-715, doi:10.1038/s41586-023-
744 06243-w (2023).
- 745 63 Hyrenius-Wittsten, A. *et al.* SynNotch CAR circuits enhance solid tumor recognition and
746 promote persistent antitumor activity in mouse models. *Sci Transl Med* **13**,
747 doi:10.1126/scitranslmed.abd8836 (2021).
- 748 64 Tousley, A. M. *et al.* Co-opting signalling molecules enables logic-gated control of CAR T
749 cells. *Nature* **615**, 507-516, doi:10.1038/s41586-023-05778-2 (2023).
- 750 65 Globerson Levin, A., Riviere, I., Eshhar, Z. & Sadelain, M. CAR T cells: Building on the
751 CD19 paradigm. *Eur J Immunol* **51**, 2151-2163, doi:10.1002/eji.202049064 (2021).
- 752 66 Gargett, T. & Brown, M. P. The inducible caspase-9 suicide gene system as a "safety
753 switch" to limit on-target, off-tumor toxicities of chimeric antigen receptor T cells. *Front*
754 *Pharmacol* **5**, 235, doi:10.3389/fphar.2014.00235 (2014).
- 755 67 Chang, S. Y. *et al.* Circulatory antigen processing by mucosal dendritic cells controls
756 CD8(+) T cell activation. *Immunity* **38**, 153-165, doi:10.1016/j.immuni.2012.09.018 (2013).
- 757 68 Koga, T. *et al.* Evidence for early aging in the mucosal immune system. *J Immunol* **165**,
758 5352-5359, doi:10.4049/jimmunol.165.9.5352 (2000).

- 759 69 Luecken, M. D. & Theis, F. J. Current best practices in single-cell RNA-seq analysis: a
760 tutorial. *Mol Syst Biol* **15**, e8746, doi:10.15252/msb.20188746 (2019).
- 761 70 Amezquita, R. A. *et al.* Orchestrating single-cell analysis with Bioconductor. *Nat Methods*
762 **17**, 137-145, doi:10.1038/s41592-019-0654-x (2020).
- 763 71 Butler, A., Hoffman, P., Smibert, P., Papalexi, E. & Satija, R. Integrating single-cell
764 transcriptomic data across different conditions, technologies, and species. *Nat Biotechnol*
765 **36**, 411-420, doi:10.1038/nbt.4096 (2018).
- 766 72 Stuart, T. *et al.* Comprehensive Integration of Single-Cell Data. *Cell* **177**, 1888-1902
767 e1821, doi:10.1016/j.cell.2019.05.031 (2019).
- 768 73 van Dijk, D. *et al.* Recovering Gene Interactions from Single-Cell Data Using Data
769 Diffusion. *Cell* **174**, 716-729 e727, doi:10.1016/j.cell.2018.05.061 (2018).
- 770 74 Finak, G. *et al.* MAST: a flexible statistical framework for assessing transcriptional changes
771 and characterizing heterogeneity in single-cell RNA sequencing data. *Genome Biol* **16**,
772 278, doi:10.1186/s13059-015-0844-5 (2015).
- 773 75 Sato, T. *et al.* Single Lgr5 stem cells build crypt-villus structures in vitro without a
774 mesenchymal niche. *Nature* **459**, 262-265, doi:10.1038/nature07935 (2009).
- 775 76 Ruscetti, M. *et al.* NK cell-mediated cytotoxicity contributes to tumor control by a cytostatic
776 drug combination. *Science* **362**, 1416-1422, doi:10.1126/science.aas9090 (2018).
- 777 77 Debacq-Chainiaux, F., Erusalimsky, J. D., Campisi, J. & Toussaint, O. Protocols to detect
778 senescence-associated beta-galactosidase (SA-beta-gal) activity, a biomarker of
779 senescent cells in culture and in vivo. *Nat Protoc* **4**, 1798-1806,
780 doi:10.1038/nprot.2009.191 (2009).
- 781 78 Cahu, J. & Sola, B. A sensitive method to quantify senescent cancer cells. *J Vis Exp*,
782 doi:10.3791/50494 (2013).
- 783 79 Kuhn, N. F. *et al.* CD40 Ligand-Modified Chimeric Antigen Receptor T Cells Enhance
784 Antitumor Function by Eliciting an Endogenous Antitumor Response. *Cancer Cell* **35**, 473-
785 488 e476, doi:10.1016/j.ccell.2019.02.006 (2019).
- 786 80 Davila, M. L., Kloss, C. C., Gunset, G. & Sadelain, M. CD19 CAR-targeted T cells induce
787 long-term remission and B Cell Aplasia in an immunocompetent mouse model of B cell
788 acute lymphoblastic leukemia. *PLoS One* **8**, e61338, doi:10.1371/journal.pone.0061338
789 (2013).
- 790 81 Brentjens, R. J. *et al.* Eradication of systemic B-cell tumors by genetically targeted human
791 T lymphocytes co-stimulated by CD80 and interleukin-15. *Nat Med* **9**, 279-286,
792 doi:10.1038/nm827 (2003).
- 793 82 Yoon, Y. M. *et al.* Gut microbiota modulates bleomycin-induced acute lung injury response
794 in mice. *Respir Res* **23**, 337, doi:10.1186/s12931-022-02264-7 (2022).
- 795

796

797

798

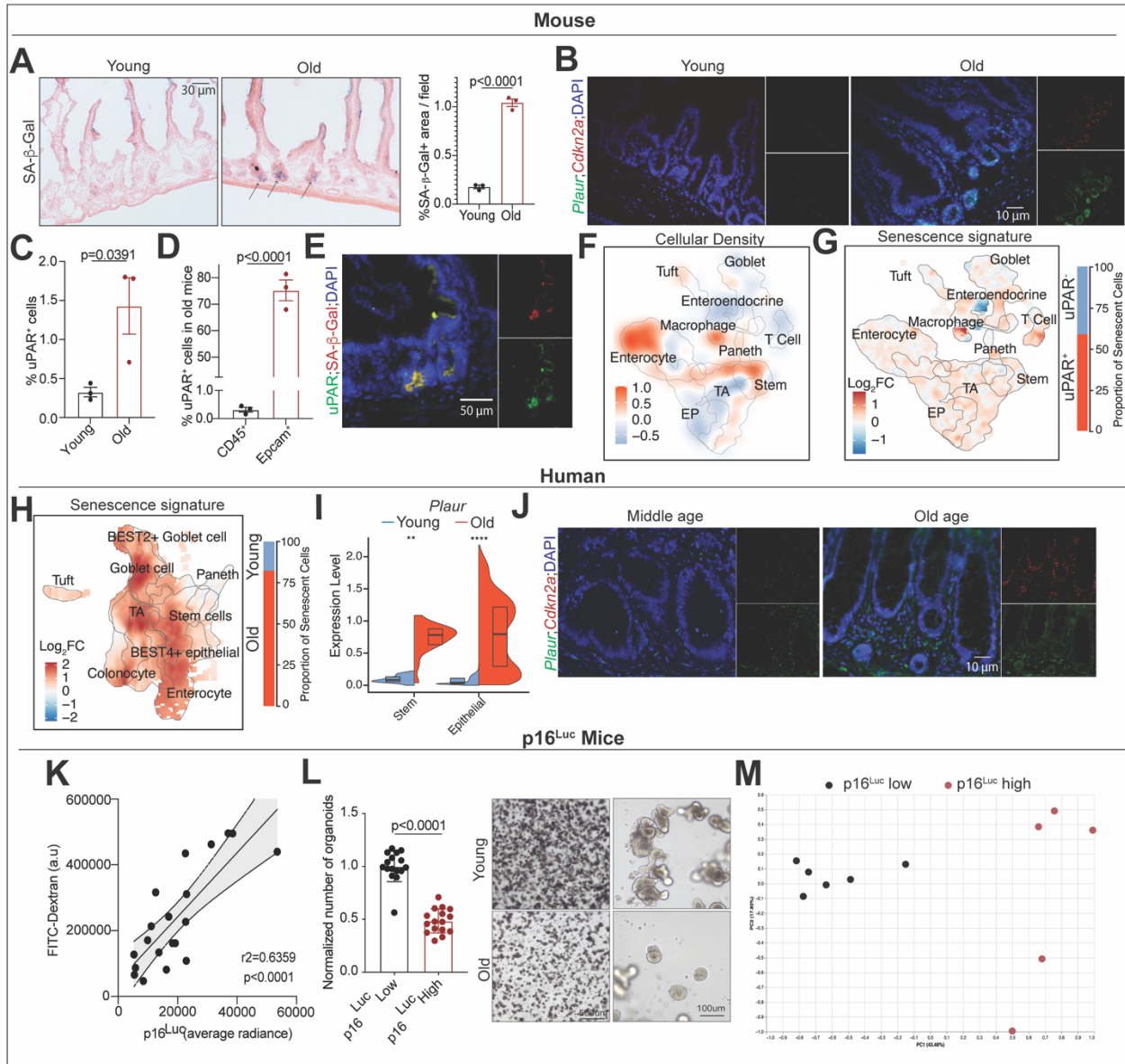
799

800

801

802 **FIGURES**

Figure 1



803

804 **Fig. 1. uPAR⁺ senescent cells accumulate in aging in murine and human intestines and**
805 **correlate with decreased intestinal fitness.**

806 **(A)** Representative SA-β-gal staining of proximal jejunum of young (3 months) and old (20
807 months) mice and quantification (right) (n=3 per group).

808 **(B)** Representative co-immunofluorescence pictures showing levels of *Plaur* and *Cdkn2a* in
809 proximal jejunum of young (3 months) and old (20 months) mice through RNA in situ hybridization.
810 (n=3 per group)

811 **(C)** Cell surface uPAR expression as determined by flow cytometry on isolated intestinal crypts
812 from young (3 months) and old (20 months) mice. (n=3 per group).

813 **(D)** Percentage of surface uPAR positive cells that are either Epcam positive or CD45 positive as
814 determined by flow cytometry on isolated intestinal crypts from young (3 months) and old (20
815 months) mice. (n=3 per group).

816 **(E)** Representative co-immunofluorescence of SA- β -gal and uPAR staining in the proximal
817 jejunum of 20 month old mice (n=3).

818 **(F-G)** uPAR⁺ and uPAR⁻ cells from isolated intestinal crypts from old (20 months old) mice were
819 FACS sorted and subjected to scRNAseq (n=4 mice per group).

820 **(F)** Uniform manifold approximation and projection (UMAP) visualization of small intestinal cell
821 types generated by 10X chromium protocol. Color scale indicates differences in density of cellular
822 populations between uPAR⁺ and uPAR⁻ cells.

823 **(G)** UMAP visualization of small intestinal cell types generated by 10X chromium protocol. Color
824 scale indicates log₂FC change in senescence signature³³ between uPAR⁺ and uPAR⁻ cells. Right:
825 quantification of the proportion of uPAR⁺ and uPAR⁻ cells contributing to the senescence
826 signature.

827 **(H)** UMAP visualization of small intestinal cell types in young (25-30 years old) and old (65-70
828 years old) subjects generated by 10X chromium protocol. Color scale indicates log₂FC change in
829 senescence signature³³ between old versus young. Right: quantification of the proportion of old
830 and young cells contributing to the senescence signature.

831 **(I)** Split-violin plot indicates the expression level *PLAUR* in the intestinal stem cell and epithelial
832 lineage of young (25-30 years old) and old (65-70 years old) subjects generated by 10X chromium
833 protocol. Boxplots display median (center line) and interquartile range (box).

834 **(J)** Representative immunofluorescence pictures showing levels of *PLAUR* and *CDKN2A* in
835 samples from the intestine of middle aged (56 years old) and old (89 years old) humans through
836 RNA in situ hybridization.

837 **(K)** Correlation between luciferase levels as measured by average radiance in p16^{Luc} mice with
838 the levels of FITC-dextran in plasma 4h after oral administration. Solid and dotted lines show
839 linear regression and 95% confidence interval. (n=20).

840 **(L)** Secondary organoid formation capacity of crypts from mice with low levels of p16Luc (<20.000
841 p/s/cm²/sr average radiance) or high levels of p16Luc (>20.000 p/s/cm²/sr average radiance) (n=2
842 mice per group, 8 replicates per mouse) quantification at day 3, representative brightfield images
843 of day 4 secondary organoids.

844 **(M)** Principal coordinate analysis (PCoA) of the microbial composition in feces of mice with low
845 levels of p16 (average radiance < 20.000 p/s/cm²/sr, n=6) and of feces from mouse with high
846 levels of p16 (average radiance > 20.000 p/s/cm²/sr, n=5).

847 (A-M) results of 1 independent experiment. (C-D, L) Data are mean \pm s.e.m. (C-D, L) Two-tailed
848 unpaired Student's t-test. (I) Wilcoxon rank sum test. *P<0.05, **P<0.01, ***P<0.001,
849 ****P<0.0001. (K) Pearson correlation coefficient.

850

851

852

853

854

855

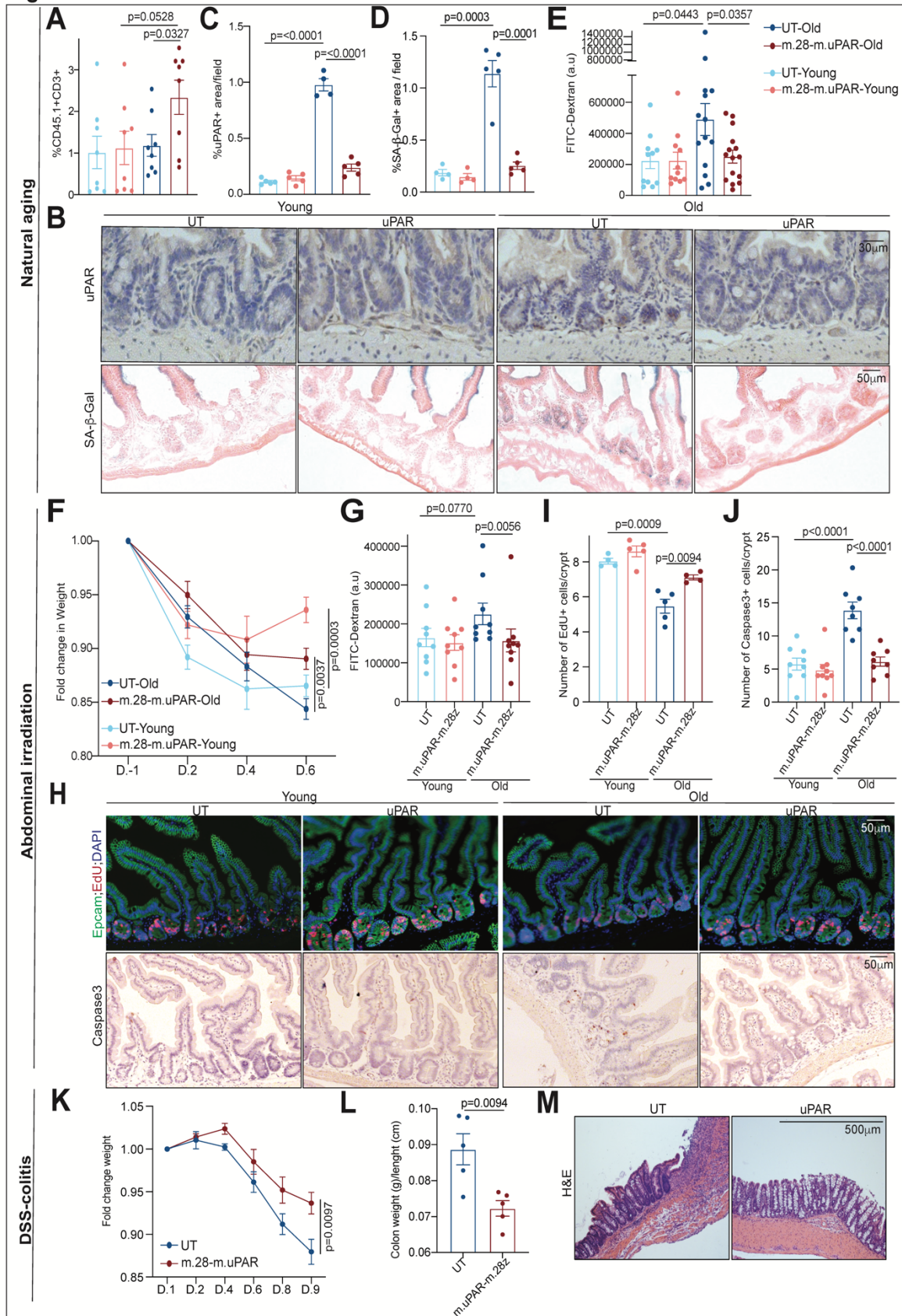
856

857

858

859

Figure 2



861 **Fig. 2. Senolytic uPAR targeting CAR T cells rescue intestinal epithelium integrity in aging**
862 **and injury.**

863 **(A-E)** Young (3 months) and old (18 months) mice were treated with 0.5×10^6 untransduced T
864 cells (UT) or uPAR CAR T cells (m.uPAR-m.28z). Mice were harvested 6 weeks after infusion.

865 **(A)** Percentage of CD45.1 and CD3 double positive cells in the intestinal crypts. (n=8 per group).

866 **(B)** Representative immunohistochemistry staining of uPAR and SA-b-gal staining of proximal
867 jejunum.

868 **(C)** Percentage of histological area with uPAR positive cells per field as determined by
869 immunohistochemistry in the proximal jejunum (n=5 for UT and m.uPAR-m.28z young; n=5
870 m.uPAR-m.28z old; n=4 for UT old).

871 **(D)** Percentage of histological area with SA- β -gal positive cells in the proximal jejunum (n=5 for
872 UT and m.uPAR-m.28z young; n=5 m.uPAR-m.28z old; n=4 for UT old).

873 **(E)** Plasma levels of FITC-Dextran 4 hours after oral gavage. (n=11 for UT and m.uPAR-m.28z
874 young; n=14 for UT old; n=15 for m.uPAR-m.28z old).

875 **(F-J)** Young (3 months) and old (18 months) mice were infused with 0.5×10^6 untransduced T
876 cells (UT) or uPAR CAR T cells (m.uPAR-m.28z). 15 days after cell injection mice were subjected
877 to abdominal irradiation with 15Gy. Mice were harvested 6 days after irradiation.

878 **(F)** Fold change in weight before and after abdominal irradiation with 15Gy. (D= day). (n=10 per
879 group).

880 **(G)** Plasma levels of FITC-Dextran 4 hours after oral gavage. (n=9 per group).

881 **(H)** Representative immunofluorescence staining of Epcam (green), EdU (red) and DAPI (blue)
882 and immunohistochemistry of Caspase 3 of proximal jejunum.

883 **(I)** Quantification of number of EdU positive cells per intestinal crypt in samples from (I). (n=4 for
884 UT young, n=5 m.uPAR-m.28z young, n=5 UT old, n=4 m.uPAR-m.28z old).

885 **(J)** Quantification of number of Caspase 3 positive cells per intestinal crypt in samples from (I).
886 (n=9 for UT and m.uPAR-m.28z young; n=8 for UT and m.uPAR-m.28z old).

887 **(K-M)** Young (3 months) mice were infused with 0.5×10^6 untransduced T cells (UT) or uPAR
888 CAR T cells (m.uPAR-m.28z). 20 days after cell injection mice were subjected to continuous
889 drinking water with 2% of DSS. Mice were harvested 9 days after the start of DSS administration.
890 **(K)** Fold change in weight before and after DSS administration. (D= day). (n=5 per group).
891 **(L)** Ratio of colon weight (g) to colon length (cm) at day 9 of DSS administration. (n=5 per group).
892 **(M)** Representative hematoxylin and eosin (H&E) staining of colons at day 9 of DSS
893 administration.
894 (A-J) results of 2 independent experiments. (K-M) results of 1 independent experiment. (A, C-G, I-
895 L) Data are mean \pm s.e.m. (A, C-F, I-J, L) two-tailed unpaired Student's t-test. (G) Mann-Whitney
896 test. (K) Two way ANOVA.

897

898

899

900

901

902

903

904

905

906

907

908

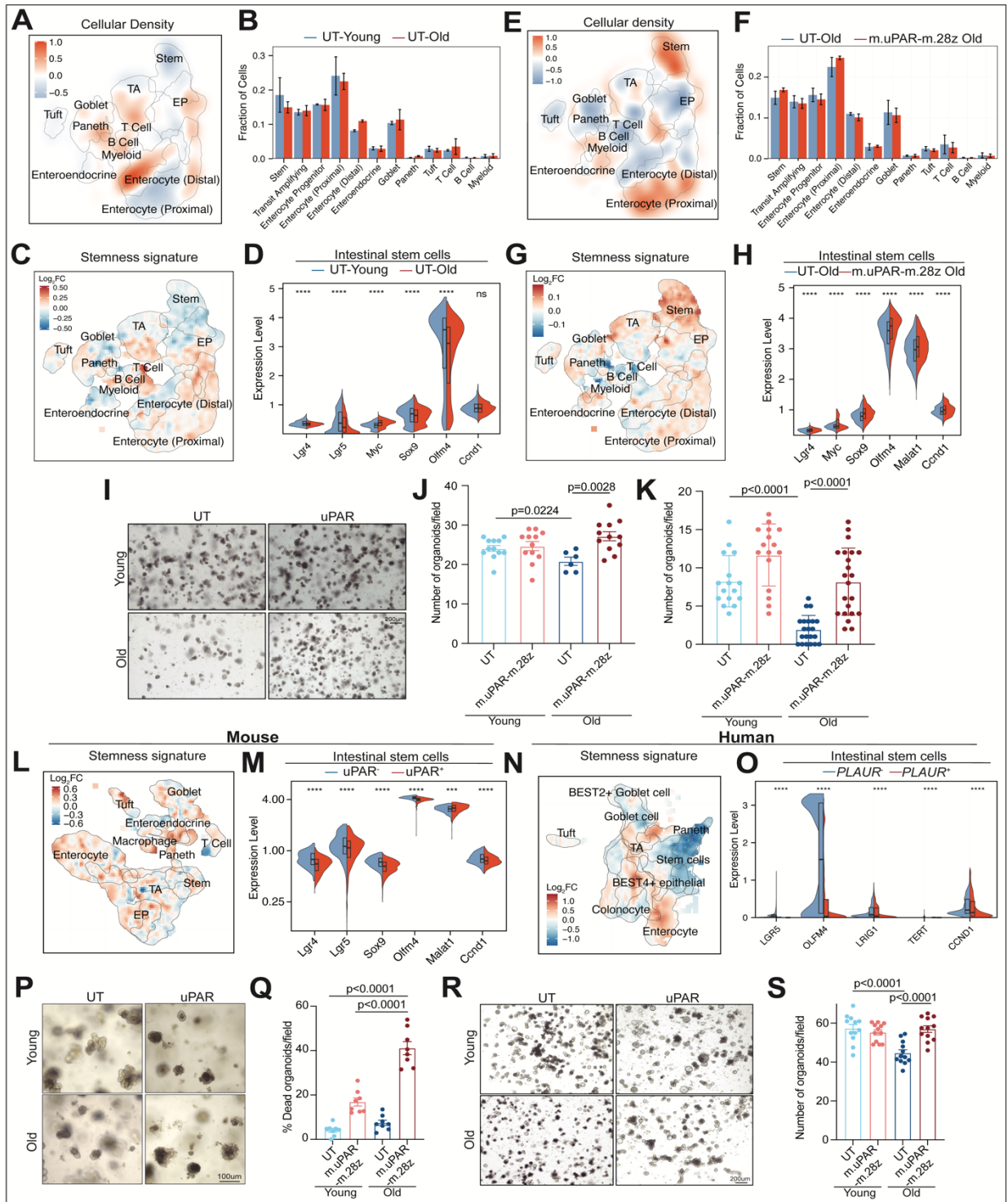
909

910

911

912

Figure 3



913

914

915

916 **Fig. 3. uPAR CAR T cells rejuvenate intestinal stem cells *in vivo* and *in vitro*.**

917 **(A-H)** Young (3 months) and old (18 months) mice were treated with 0.5×10^6 untransduced T
918 cells (UT) or uPAR CAR T cells (m.uPAR-m.28z). Mice were harvested 6 weeks after infusion.

919 **(A)** UMAP visualization of small intestinal cell types generated by 10X chromium protocol. Color
920 scale indicates difference in localized cellular density between UT treated old and young mice.
921 (n=4 mice per group).

922 **(B)** Fraction of cells for each of the different cell types shown in (A) in UT treated old and young
923 mice (n=4 mice per group). Error bars represent s.e.m.

924 **(C)** UMAP visualization of small intestinal cell types generated by 10X chromium protocol. Color
925 scale indicates \log_2 FC differences in stemness signature score between UT treated old and
926 young mice (n=4 mice per group).

927 **(D)** Split-violin plot indicates the expression level of 6 different stem-related genes in the stem
928 cells from UT treated old and young mice. (n=4 mice per group). Boxplots display median (center
929 line) and interquartile range (box).

930 **(E)** UMAP visualization of small intestinal cell types generated by 10X chromium protocol. Color
931 scale indicates difference in localized cellular density between uPAR and UT CAR T treated old
932 mice. (n=4 mice per group).

933 **(F)** Fraction of cells for each of the different cell types shown in (E) in old mice treated with UT or
934 uPAR CAR T cells. (n=4 mice per group). Error bars represent s.e.m.

935 **(G)** UMAP visualization of small intestinal cell types generated by 10X chromium protocol. Color
936 scale indicates \log_2 FC differences in stemness signature score between uPAR CAR T and UT
937 treated old mice. (n=4 mice per group).

938 **(H)** Split-violin plot indicates the expression level of 6 different stem-related genes in the stem
939 cells from old UT and uPAR CAR T treated mice. (n=4 mice per group). Boxplots display median
940 (center line) and interquartile range (box).

941 **(I-K)** Young (3 months) and old (18 months) mice were treated with 0.5×10^6 untransduced T
942 cells (UT) or uPAR CAR T cells (m.uPAR-m.28z). Mice were harvested 8 weeks after infusion and
943 organoids were generated from their crypts.

944 **(I-J)** Organoid initiating capacity of crypts from young or old, UT or uPAR CAR T treated mice
945 (n=2 mice per group, 6 replicates per mouse). **(I)** Representative images of day 5 secondary
946 organoids. **(J)** Number of secondary organoids on day 4 per dissociated crypt-derived primary
947 organoid.

948 **(K)** Organoid initiating capacity on day 4 of sorted Epcam+ cells from the intestinal crypts of young
949 and old, UT or uPAR CAR T treated mice (n=4 mice per group).

950 **(L)** UMAP visualization of murine small intestinal cell types generated by 10X chromium protocol.
951 Color scale indicates log₂FC differences in stemness signature score between mouse uPAR
952 positive and uPAR negative cells. (n=4 mice per group).

953 **(M)** Split-violin plot indicates the expression level of 6 different stem-related genes in mouse uPAR
954 positive or uPAR negative stem cells. (n=4 mice per group). Boxplots display median (center line)
955 and interquartile range (box).

956 **(N)** UMAP visualization of human small intestinal cell types generated by 10X chromium protocol.
957 Color scale indicates log₂FC differences in stemness signature score between human *PLAUR*
958 positive and *PLAUR* negative cells. (n=4 mice per group).

959 **(O)** Split-violin plot indicates the expression level of 5 different stem-related genes in human
960 *PLAUR* positive or *PLAUR* negative stem cells. (n=4 mice per group). Boxplots display median
961 (center line) and interquartile range (box).

962 **(P-S)** Intestinal crypts from young (3 months) and old (20 months old) mice were isolated and
963 seeded to form organoids together with either UT or m.uPAR-m28z cells at 1:10 effector:target
964 ratio. 72h later equal numbers of secondary organoids were generated per dissociated crypt-
965 derived primary organoids.

966 **(P)** Representative images of organoids and UT or m.uPAR-m28z CAR T cell co-culture. (n=8
967 replicates).

968 **(Q)** Quantification of the percentage of dead organoids per field 72h after co-culture between
969 organoids and UT or m.uPAR-m28z CAR T cells. (n= 8 replicates).

970 **(R)** Representative images of secondary organoids from young and old in vitro UT or m.uPAR-
971 m28z CAR T cell treated primary organoids. (n=12 replicates).

972 **(S)** Quantification of number of secondary organoids on day 4. (n=12 replicates).

973 (A-O) results of 1 independent experiment. (P-S) results of 2 independent experiments. (D,H,M,O)

974 Wilcoxon rank-sum test *P<0.05, **P<0.01, ***P<0.001, ****P<0.0001. (J,K,Q,S) Data are mean

975 \pm s.e.m. (J,K,Q,S) two-tailed unpaired Student's t-test.

976

977

978

979

980

981

982

983

984

985

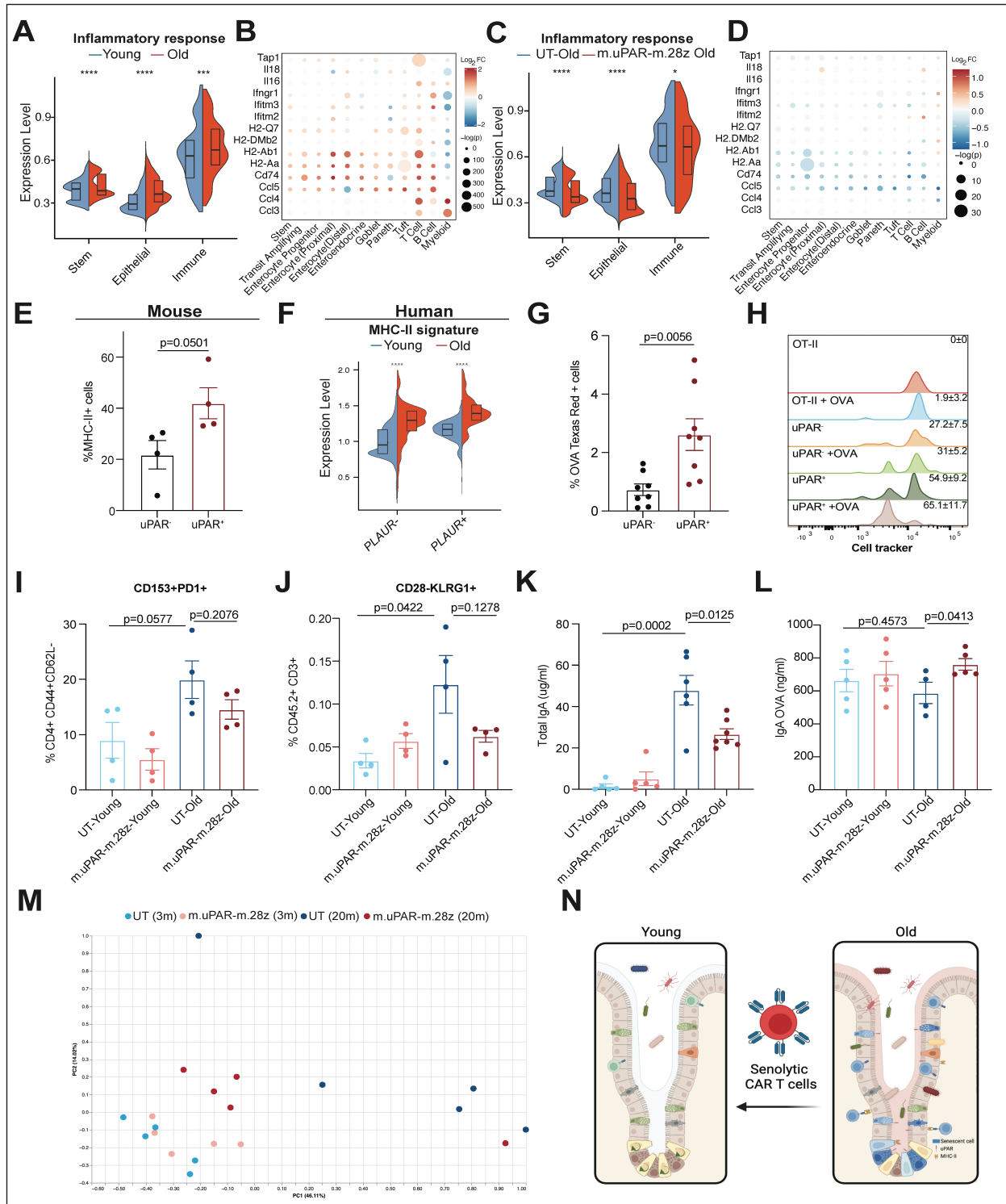
986

987

988

989

Figure 4



990

991

992 **Fig. 4. Senescent cells drive chronic age-related intestinal inflammation.**

993 **(A)** Split-violin depicting the log₂ fold change in the levels of key genes in the inflammatory
994 response signature across cell types in old UT mice versus young UT infused mice 6 weeks post
995 infusion. (n=4 mice per group). Boxplots display median (center line) and interquartile range (box).

996 **(B)** Dotplot indicates the expression level of the different genes of the inflammatory response
997 signature for the different cell types in old UT mice versus young UT infused mice 6 weeks after
998 infusion. (n=4 mice per group).

999 **(C)** Split-violin depicting the log₂ fold change in the levels of key genes in the inflammatory
1000 response signature across cell types in old uPAR CAR T treated mice versus old UT infused mice
1001 6 weeks post infusion. (n=4 mice per group). Boxplots display median (center line) and
1002 interquartile range (box).

1003 **(D)** Dotplot indicates the expression level of the different genes of the inflammatory response
1004 signature for the different cell types in old uPAR CAR T treated mice vs old UT infused mice 6
1005 weeks after infusion. (n=4 mice per group).

1006 **(E)** Percentage of cells expressing surface MHC-II as determined by flow cytometry on CD45⁻
1007 Epcam⁺ uPAR⁻ or uPAR⁺ cells on isolated intestinal crypts from old (18 months old) mice. (n=4 per
1008 group).

1009 **(F)** Split-violin plot indicates the expression level of MHC-II signature score in epithelial and stem
1010 *PLAUR*⁻ or *PLAUR*⁺ cells from the ileum of young (25-30 years old) and old (65-70 years old)
1011 subjects. Boxplots display median (center line) and interquartile range (box).

1012 **(G)** 18 months old mice were administered 1mg/ml ovalbumin conjugated to Texas red by oral
1013 gavage. Intestinal crypts were isolated and dissociated 1h after administration. Graph depicting
1014 percentage of cells CD45⁻ Epcam⁺ uPAR⁻ or uPAR⁺ cells positive for Texas red. (n=8 mice per
1015 group).

1016 **(H)** CD45⁻ Epcam⁺ uPAR⁺ cells induce CD4⁺ T cell proliferation *in vitro*. Representative FACS
1017 histograms of cell trace violet-labeled CD4⁺ T cells from OT-II mice that were cultured alone or

1018 with CD45⁻ Epcam⁺ uPAR⁻ or CD45⁻ Epcam⁺ uPAR⁺ cells from 18 month old mice with or without
1019 15ug/ml of OVA323-339. Values shown are mean \pm s.d. (n=4 mice per group).

1020 **(I)** Percentage of senescent endogenous T cells (CD153+PD1+) from CD4+CD44+CD62L- T cells
1021 in the intestinal crypts of young and old mice 6 weeks after cell infusion. (n=4 per group).

1022 **(J)** Percentage of senescent endogenous T cells (CD28- KLRG1+) from total CD45.2+ CD3+ cells
1023 in the intestinal crypts of young and old mice 6 weeks after cell infusion. (n=4 per group).

1024 **(JK)** Serum levels of total unspecific IgA in young and old mice 20 days after cell infusion (young
1025 UT n=5, young uPAR n=5, old UT n=6 mice, old uPAR n=7 mice).

1026 **(L)** Young (3m) and old (20m) mice were infused with 0.5×10^6 UT or m.uPAR-m.28z CAR T cells.
1027 20 days after infusion, mice were immunized by oral gavage with OVA and cholera toxin on three
1028 occasions separated by 7 days. Serum was collected on day 21 and levels of specific anti OVA
1029 IgA were determined by ELISA. (Young UT n=5, young uPAR n=5, old UT n=4 mice, old uPAR
1030 n=5 mice).

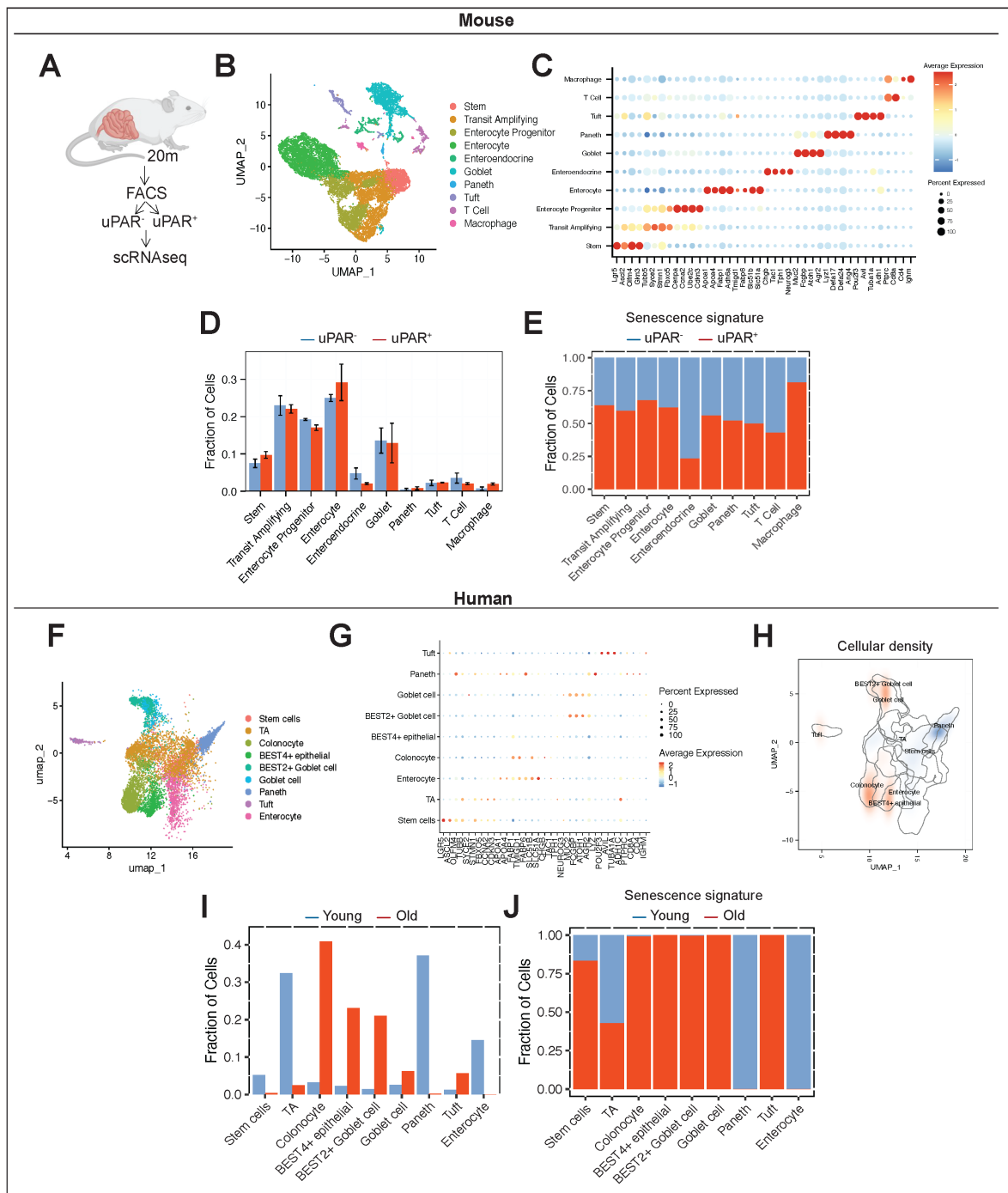
1031 **(M)** Principal coordinate analysis (PCoA) of the microbial composition in fecal samples of young
1032 (3m) and old (20m) mice 20 days after infusion with 0.5×10^6 UT or m.uPAR-m.28z CAR T cells
1033 (n=5 mice per group).

1034 **(N)** Summary of the key points of our findings. Senescent cells (blue) of different lineages
1035 accumulate in the small intestine with age. They express surface uPAR (red molecule). Senescent
1036 cells lead to decreased intestinal fitness characterized by reduced ISC activity and decreased
1037 epithelial barrier integrity. Through expression of MHC-II molecules, senescent cells contribute to
1038 chronic immune activation and mucosal immune senescence. Treatment with anti-uPAR CAR T
1039 cells eliminates senescent cells and rejuvenates the overall fitness of the small intestine.

1040 (A-F, H-M) results of 1 independent experiment. (G) results of 2 independent experiments. (E,G,
1041 I-L) Data are mean \pm s.e.m. (H) Data are mean \pm s.d. (A,C,F) Wilcoxon rank sum test
1042 *P<0.05, **P<0.01, ***P<0.001, ****P<0.0001. (B, D, E,G, I-L) Two-tailed unpaired Student's t-test.

1043 **FIGURE S1 (RELATED TO FIGURE 1)**
 1044

Supplementary Figure 1



1045 **Figure S1. Age-dependent accumulation and characteristics of uPAR⁺ senescent cells in**
 1046 **murine and human small intestines. Related to Figure 1.**
 1047
 1048

1049 **(A)** Experimental scheme for (B-F and Fig.1F-G) . uPAR⁺ and uPAR⁻ cells from isolated intestinal
1050 crypts from old (20 months old) mice were FACS sorted and subjected to scRNAseq (n=4 mice
1051 per group).

1052 **(B)** Uniform manifold approximation and projection (UMAP) visualization of small intestinal cell
1053 types generated by 10X chromium protocol. Colors indicate the 10 different intestinal epithelial
1054 lineages.

1055 **(C)** Dot plot showing the 40 signature gene expressions across the 10 lineages. The size of the
1056 dots represents the proportion of cells expressing a particular marker, and the color scale
1057 indicates the mean expression levels of the markers (log₁p transformed).

1058 **(D)** Bar graph representing the fraction of cells in each of the 10 different populations on uPAR⁺
1059 and uPAR⁻ cells from isolated intestinal crypts from old (20 months old) mice. Error bars represent
1060 s.e.m.

1061 **(E)** Quantification of the proportion of uPAR⁺ and uPAR⁻ cells by cell type contributing to the
1062 senescence signature in Fig.1G.

1063 **(F)** UMAP visualization of human ileal cell types generated by 10X chromium protocol. Colors
1064 indicate the 9 different intestinal epithelial lineages.

1065 **(G)** Dot plot showing the 33 signature gene expressions across the 9 lineages. The size of the
1066 dots represents the proportion of cells expressing a particular marker, and the color scale
1067 indicates the mean expression levels of the markers (log₁p transformed).

1068 **(H)** UMAP visualization of human ileal cell types generated by 10X chromium protocol. Color scale
1069 indicates differences in density of cellular populations between old (65-70 years old) and young
1070 (25-30 years old) subjects.

1071 **(I)** Bar graph representing the fraction of cells in each of the 9 different populations on ileal cells
1072 from young (25-30 years old) and old (65-70 years old) subjects.

1073 **(J)** Quantification of the proportion old and young cells by cell type contributing to the senescence
1074 signature in **(Fig.1H)**.

1075 (A-J) results of 1 independent experiment.

1076

1077

1078

1079

1080

1081

1082

1083

1084

1085

1086

1087

1088

1089

1090

1091

1092

1093

1094

1095

1096

1097

1098

1099

1100

1101

1102

1103

1104

1105

1106

1107

1108

1109

1110

1111

1112

1113

1114

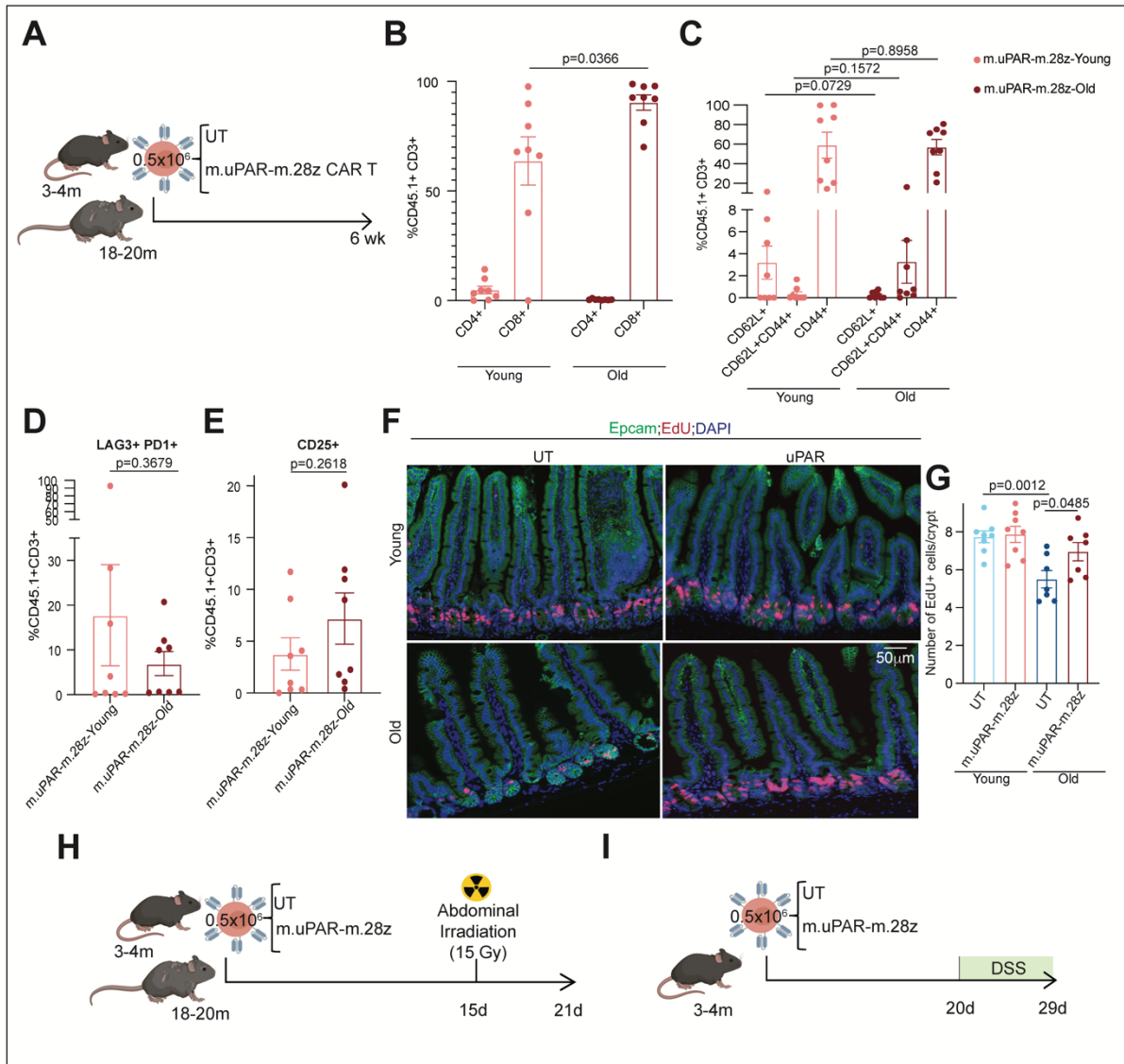
1115

1116

1117

1118 **FIGURE S2 (RELATED TO FIGURE 2)**
 1119

Figure S2



1120
 1121

1122 **Figure S2. Profile and effect of uPAR targeting CAR T cells in aged and injured small**
 1123 **intestine. Related to Figure 2.**

1124 **(A)** Experimental scheme for (Figure 2A-E and S2B-G). Young (3 months) and old (18-20 months)
 1125 mice were treated with 0.5×10^6 untransduced T cells (UT) or uPAR CAR T cells (m.uPAR-m.28z).
 1126 Mice were harvested 6 weeks after infusion.

1127 **(B)** Percentage of CD4 positive or CD8 positive cells from CD45.1 and CD3 double positive cells
1128 in the intestinal crypts. (n=8 per group).

1129 **(C)** Percentage of CD62L, CD44 and CD62L and CD44 positive cells from CD45.1 and CD3
1130 double positive cells in the intestinal crypts. (n=8 per group).

1131 **(D)** Percentage of LAG3 and PD1 positive cells from CD45.1 and CD3 double positive cells in the
1132 intestinal crypts. (n=8 per group).

1133 **(E)** Percentage of CD25 positive cells from CD45.1 and CD3 double positive cells in the intestinal
1134 crypts. (n=8 per group).

1135 **(F)** Representative immunofluorescence staining of Epcam (green), EdU (red) and DAPI (blue) of
1136 proximal jejunum.

1137 **(G)** Quantification of number of EdU positive cells per intestinal crypt in samples from (J).(n=8 for
1138 UT and m.uPAR-m.28z young and n=7 for UT and m.uPAR-m.28z old).

1139 **(H)** Experimental scheme for (Figure 2F-J and S2I). Young (3 months) and old (18 months) mice
1140 were infused with 0.5×10^6 untransduced T cells (UT) or uPAR CAR T cells (m.uPAR-m.28z). 15
1141 days after cell injection mice were subjected to abdominal irradiation with 15Gy. Mice were
1142 harvested 6 days after irradiation.

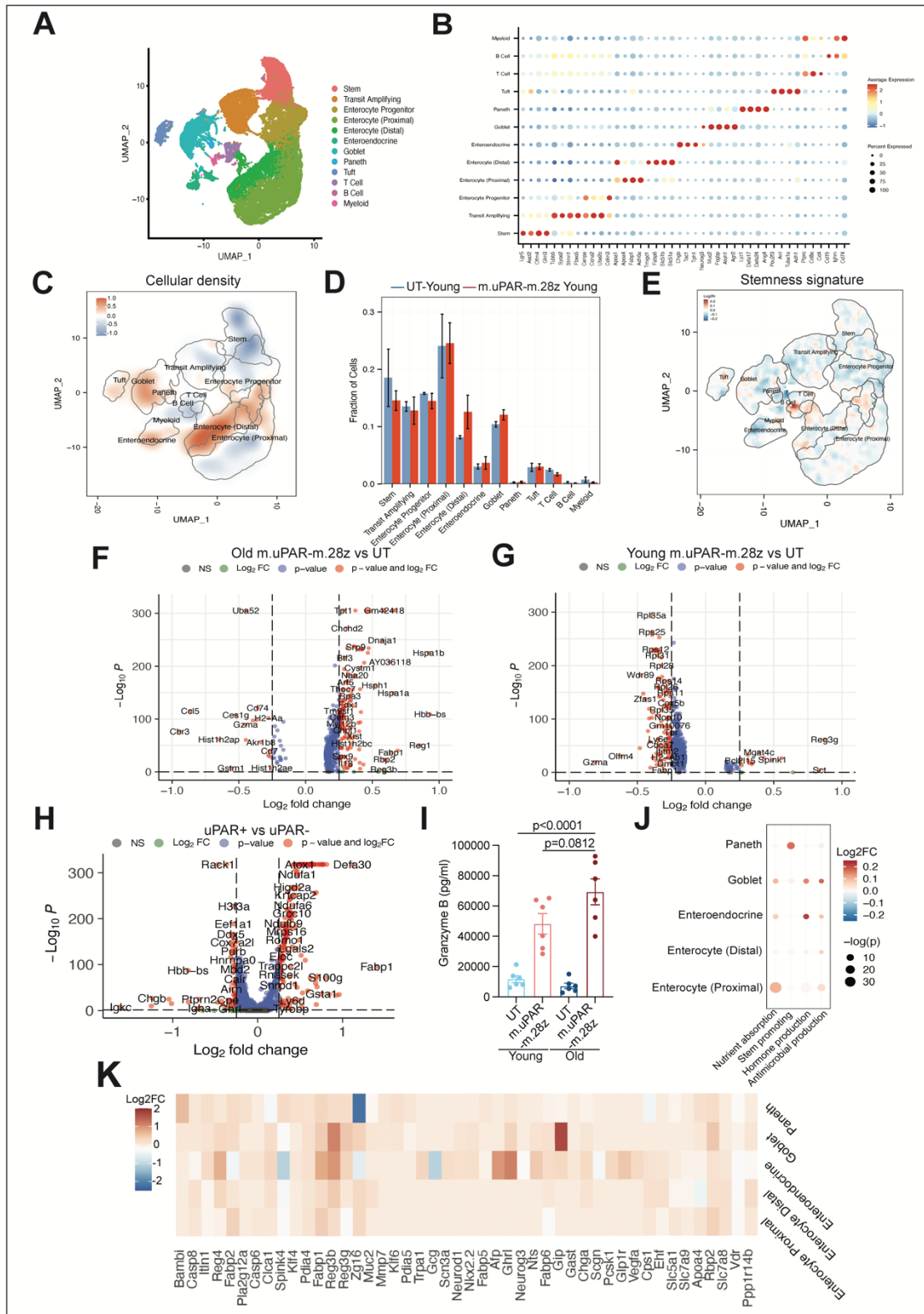
1143 **(I)** Experimental scheme for (Figure 2K-M). Young (3 months) mice were infused with 0.5×10^6
1144 untransduced T cells (UT) or uPAR CAR T cells (m.uPAR-m.28z). 20 days after cell injection mice
1145 were subjected to continuous drinking water with 2% of DSS. Mice were harvested 9 days after
1146 the start of DSS administration.

1147 (B-E) results from 2 independent experiments. (F-G) results from 1 independent experiment. (B-
1148 E, G) Data are mean \pm s.e.m. (B-E, G) two-tailed unpaired Student's t-test.

1149
1150
1151
1152
1153
1154

1155 **FIGURE S3 (RELATED TO FIGURE 3)**

Figure S3



1157 **Figure S3. Effect of uPAR-targeting CAR T cells on intestinal crypts. Related to Figure 3.**

1158 **(A-G)** Young (3 months) and old (18-20 months) mice were treated with 0.5×10^6 untransduced
1159 T cells (UT) or uPAR CAR T cells (m.uPAR-m.28z). Mice were harvested 6 weeks after infusion.

1160 **(A)** UMAP visualization of small intestinal cell types in young (3 months old) and old (20 months
1161 old) mice treated with 0.5×10^6 untransduced T cells (UT) or uPAR CAR T cells (m.uPAR-m.28z)
1162 generated by 10X chromium protocol. Colors indicate the 12 different identified populations.

1163 **(B)** Dot plot showing the 40 signature gene expressions across the 12 cellular clusters. The size
1164 of the dots represents the proportion of cells expressing a particular marker, and the color scale
1165 indicates the mean expression levels of the markers (log_{1p} transformed).

1166 **(C)** UMAP visualization of small intestinal cell types generated by 10X chromium protocol. Color
1167 scale displays differences in cellular density of the different populations between uPAR and UT
1168 CAR T treated young mice (n=4 mice per group).

1169 **(D)** Fraction of cells for each lineage depicted in (A) for young mice treated with UT or uPAR CAR
1170 T cells. (n=4 mice per group). Error bars represent s.e.m.

1171 **(E)** UMAP visualization of small intestinal cell types generated by 10X chromium protocol. Color
1172 scale indicates log₂FC difference in stemness signature score between uPAR CAR T and UT
1173 treated young mice. (n=4 mice per group).

1174 **(F)** Volcano plot of differentially expressed genes between old mice treated with UT or uPAR CAR
1175 T cells. (n=4 mice per group).

1176 **(G)** Volcano plot of differentially expressed genes between young mice treated with UT or uPAR
1177 CAR T cells. (n=4 mice per group).

1178 **(H)** Volcano plot of differentially expressed genes between uPAR⁺ and uPAR⁻ cells. (n=4 mice per
1179 group).

1180 **(I)** Levels of granzyme B 72h after co-culture between organoids and UT or m.uPAR-m28z CAR
1181 T cells. (n= 6 replicates).

1182 **(J)** Bubble plot showing Log₂ fold change in the functional scores for the different terms across
1183 Paneth, goblet, enteroendocrine and enterocytes of old mice treated with UT or uPAR CAR T
1184 cells. (n=4 mice per group).

1185 **(K)** Heatmap representing log₂FC in gene expression between old uPAR and old UT treated
1186 mice from (I).

1187 (A-H, J-K) results of 1 independent experiment. (I) results of 2 independent experiments. (I) two-
1188 tailed unpaired Student's t-test. (F-H) MAST method.

1189

1190

1191

1192

1193

1194

1195

1196

1197

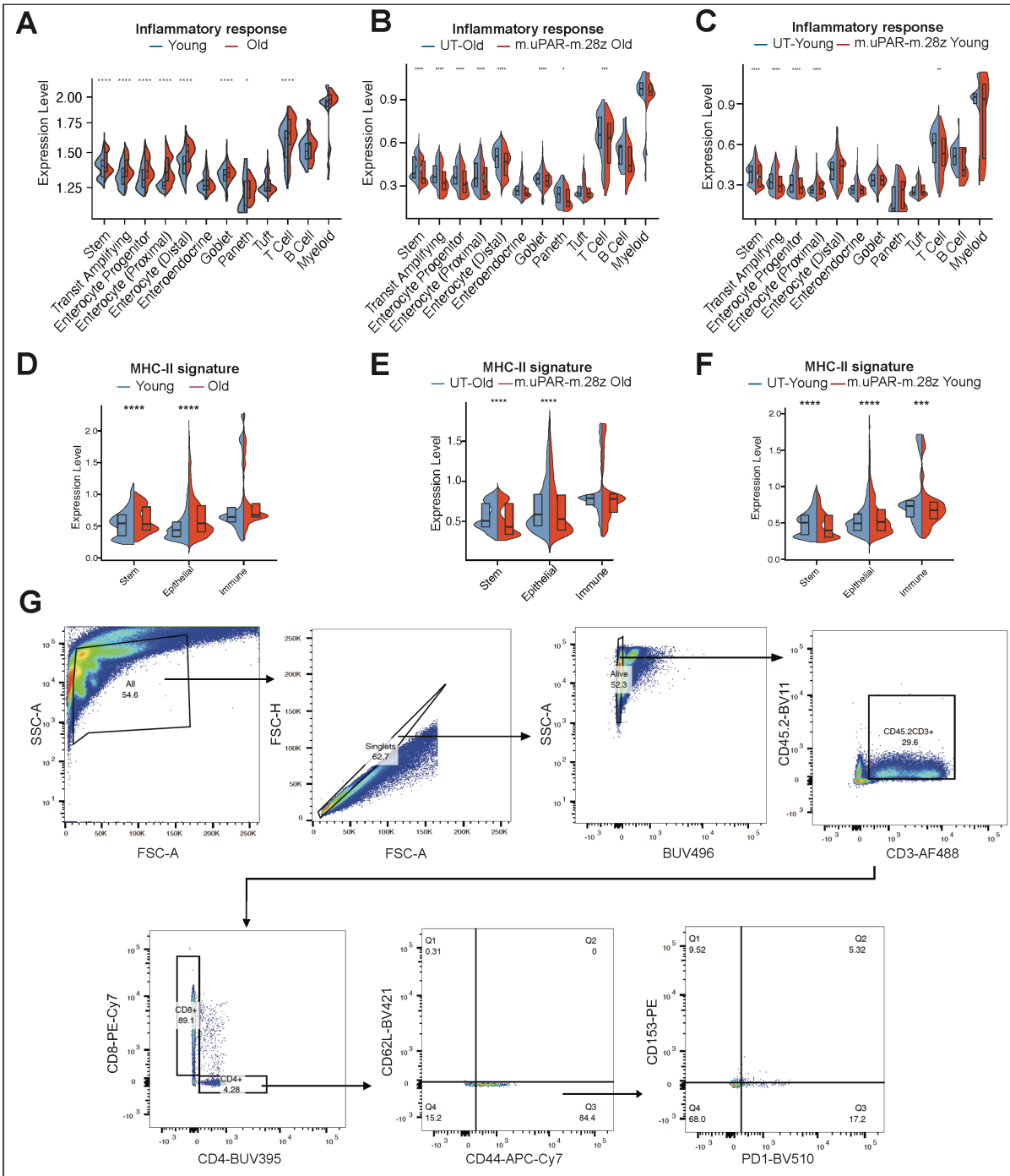
1198

1199

1200

1201

1202 **FIGURE S4 (RELATED TO FIGURE 4)**
Figure S4



1203

1204 **Fig. S4. Senolytic CAR T cells abrogate age-related intestinal inflammation. Related to**

1205 **Figure 4.**

1206 **(A)** Split-violin plot indicates the expression level of the inflammatory response signature for the
1207 different cell types in young UT and old UT mice. (n=4 mice per group). Boxplots display median
1208 (center line) and interquartile range (box).

1209 **(B)** Split-violin plot indicates the expression level of the inflammatory response signature for the
1210 different cell types in old UT and uPAR CAR T treated mice. (n=4 mice per group). Boxplots
1211 display median (center line) and interquartile range (box).

1212 **(C)** Split-violin plot indicates the expression level of the inflammatory response signature for the
1213 different cell types in young UT and uPAR CAR T treated mice. (n=4 mice per group). Boxplots
1214 display median (center line) and interquartile range (box).

1215 **(D)** Split-violin depicting the log₂ fold change in the levels of key genes in the MHC-II signature
1216 across cell types in young UT versus old UT infused mice 6 weeks post infusion. (n=4 mice per
1217 group). Boxplots display median (center line) and interquartile range (box).

1218 **(E)** Split-violin depicting the log₂ fold change in the levels of key genes in the MHC-II signature
1219 across cell types in old uPAR CAR T treated mice versus old UT infused mice 6 weeks post
1220 infusion. (n=4 mice per group). Boxplots display median (center line) and interquartile range (box).

1221 **(F)** Split-violin depicting the log₂ fold change in the levels of key genes in the MHC-II signature
1222 across cell types in young uPAR CAR T treated mice versus young UT infused mice 6 weeks post
1223 infusion. (n=4 mice per group). Boxplots display median (center line) and interquartile range (box).

1224 **(G)** Representative flow cytometry staining of senescent endogenous T cells (CD153+PD1+) from
1225 CD4+CD44+CD62L- T cells in the intestinal crypts of a young untransduced treated mice weeks
1226 after cell infusion (n=4 mice per group).

1227 (A-D) results of 1 independent experiment. (A-C) Wilcoxon rank sum test. *P<0.05,**P<0.01,
1228 ***P<0.001, ****P<0.0001.

1229